Contributions to the Surface Downwelling Longwave Irradiance during Arctic Winter at Utqiaġvik (Barrow), Alaska

G. ALEXANDER SOKOLOWSKY,[a,b] EUGENE E. CLOTHIAUX,[b] CORY F. BAGGETT,[a,b,c] SUKYOUNG LEE,[b] STEVEN B. FELDSTEIN,[b] EDWIN W. ELORANTA,[d] MARIA P. CADEDDU,[e] NITIN BHARADWAJ,[f] AND KAREN L. JOHNSON[g]

[a] *Department of Atmospheric Science, Colorado State University, Fort Collins, Colorado*
[b] *Department of Meteorology and Atmospheric Science, The Pennsylvania State University, University Park, Pennsylvania*
[c] *NWS/NCEP/Climate Prediction Center, and Innovim, LLC, College Park, Maryland*
[d] *Space Science and Engineering Center, University of Wisconsin–Madison, Madison, Wisconsin*
[e] *Climate and Atmospheric Science Department, Environmental Science Division, Argonne, National Laboratory, Lemont, Illinois*
[f] *Atmospheric Measurement and Data Sciences, Pacific Northwest National Laboratory, Richland, Washington*
[g] *Environmental and Climate Sciences Department, Brookhaven National Laboratory, Upton, New York*

(Manuscript received 19 December 2018, in final form 23 January 2020)

ABSTRACT

Intrusions of warm, moist air into the Arctic during winter have emerged as important contributors to Arctic surface warming. Previous studies indicate that temperature, moisture, and hydrometeor enhancements during intrusions all make contributions to surface warming via emission of radiation down to the surface. Here, datasets from instrumentation at the Atmospheric Radiation Measurement User Facility in Utqiaġvik (formerly Barrow) for the six months from November through April for the six winter seasons of 2013/14–2018/19 were used to quantify the atmospheric state. These datasets subsequently served as inputs to compute surface downwelling longwave irradiances via radiative transfer computations at 1-min intervals with different combinations of constituents over the six winter seasons. The computed six winter average irradiance with all constituents included was 205.0 W m^{-2}, close to the average measured irradiance of 206.7 W m^{-2}, a difference of −0.8%. During this period, water vapor was the most important contributor to the irradiance. The computed average irradiance with dry gas was 71.9 W m^{-2}. Separately adding water vapor, liquid, or ice to the dry atmosphere led to average increases of 2.4, 1.8, and 1.6 times the dry atmosphere irradiance, respectively. During the analysis period, 15 episodes of warm, moist air intrusions were identified. During the intrusions, individual contributions from elevated temperature, water vapor, liquid water, and ice water were found to be comparable to each other. These findings indicate that all properties of the atmospheric state must be known in order to quantify the radiation coming down to the Arctic surface during winter.

1. Introduction

Water vapor, liquid-water clouds, ice-water clouds, and precipitation all contribute to surface downwelling longwave irradiance in the Arctic during winter. There is an emerging body of literature indicating that the surface downwelling longwave irradiance is associated with amplified planetary-scale Rossby waves that divert synoptic-scale systems northward, producing warm, moist air intrusions that play an important role in warming the Arctic surface during winter (Doyle et al. 2011; Lee et al. 2011; Yoo et al. 2012; Skific and Francis 2013; Woods et al. 2013; Park et al. 2015; Woods and Caballero 2016; Flournoy et al. 2016; Graversen and Burtu 2016; Baggett et al. 2016; Gong et al. 2017; Lee et al. 2017). Because these intrusions are accompanied by dry air, water vapor, liquid hydrometeors, and ice hydrometeors, it is important to gain knowledge on their relative contributions to the surface downwelling longwave irradiance.

Based on available cloud climatologies and hydrometeor property parameterizations, Curry and Ebert (1992) showed that low-altitude (below approximately 3 km) ice-water hydrometeors are important in the Arctic winter. Omission of ice-water hydrometeors in their radiative transfer calculations led to underestimates of about 40 W m^{-2} in the surface downwelling

Supplemental information related to this paper is available at the Journals Online website: https://doi.org/10.1175/JCLI-D-18-0876.s1.

Corresponding author: Eugene E. Clothiaux, eec3@psu.edu

DOI: 10.1175/JCLI-D-18-0876.1

longwave irradiance. In their study, making liquid-water clouds opaque relative to their expected values increased the surface downwelling longwave irradiance by about 25 W m^{-2} in winter, illustrating that wintertime liquid-water clouds are important and not always optically thick. Curry et al. (1995) investigated clear-sky water vapor influences on surface downwelling longwave irradiance, finding that in winter there is often so little water vapor that small increases in vapor lead to large changes in the surface downwelling longwave irradiance. Together, these results indicate that water vapor, liquid-water clouds, and ice-water hydrometeors are all important contributors to the surface downwelling longwave irradiance in the Arctic winter.

Using the comprehensive cloud and radiation datasets collected during the Surface Heat Budget of the Arctic (SHEBA) experiment, Shupe and Intrieri (2004) found that liquid-water clouds dominate the surface downwelling longwave irradiance in summer, whereas both liquid hydrometeors and ice hydrometeors are important in winter. They further showed that atmospheric columns containing liquid water contribute much more to the surface downwelling longwave irradiance than do columns with only ice water. However, they did not attempt to assess water vapor and ice-hydrometeor contributions to the increase in surface downwelling longwave irradiance during times in winter when liquid-water clouds were present.

During a warm, moist, and cloudy intrusion event from 1 to 12 January 1998 over the SHEBA experimental site, Persson et al. (2017; their Fig. 8) found enhancements of 60–100 W m^{-2} in surface downwelling longwave irradiance during cloudy periods. Characterizing the impact of water vapor changes on the surface longwave downwelling irradiance was not a focus of their study. Nevertheless, their Figs. 6a and 6b are interesting in this regard as they indicate a clear sky increase of about 20–30 W m^{-2} from the beginning of 1 January 1998 to the beginning of 6 January 1998 as a result of column temperature and moisture increases, suggesting that water vapor potentially played an important role. In terms of cloud impacts during the Arctic winter, their Fig. 11a shows that the total water path contributes substantially (perhaps up to ~135 W m^{-2}) to the surface longwave downwelling irradiance. Separating the contributions into liquid and ice water only (their Fig. 11b), they found that for the same water path, liquid had a bigger impact on the surface downwelling longwave irradiance as compared to ice, and downwelling irradiances were much more scattered in value for a fixed ice water path. They speculated that this scatter might be the result of a larger range of temperatures throughout thicker ice layers as compared to liquid layers. This is one possibility, as is differing amounts of water vapor in the layers. In their study, the largest water paths were attained by ice and they matched the increases in surface downwelling longwave irradiance for the largest liquid water paths. Moreover, comparing their Figs. 11b and 11a leads to the possibility that the smallest water paths, where the surface downwelling longwave irradiance is most sensitive to water path, were the result of ice and many of the points in Fig. 11a were from mixed-phase columns and absent from Fig. 11b. All of these results attest to the importance of liquid and ice water, as well as temperature and vapor, on the surface downwelling longwave irradiance.

The study by Doyle et al. (2011) showed the critical role water vapor plays in enhancing surface downwelling longwave irradiance during the winter. They estimated that an intrusion of warm, moist air over Eureka from 9 to 11 February 2010 led to an increase of 17 W m^{-2} in the surface downwelling longwave irradiance with the temperature and water vapor each contributing to about half of the increase. Clouds contributed an additional 9 W m^{-2} to the surface downwelling longwave irradiance for the case study period. They estimated that 29 intrusions occurred from 2007 to 2011, leading to an average increase of 19 W m^{-2} in the surface downwelling longwave irradiance as a result of moisture and temperature increases alone. However, Doyle et al. (2011) did not characterize liquid- or ice-hydrometeor contributions (relative to the vapor and temperature) to the surface downwelling longwave irradiance.

While the aforementioned studies focused on the Arctic, Town et al. (2005) analyzed observations collected at the South Pole. Their results demonstrated that contributions of water vapor, temperature, and hydrometeors to the surface downwelling longwave irradiance are also important in the extremely dry South Pole atmosphere, not just the Arctic.

These prior studies demonstrated that water vapor, liquid hydrometeors, and ice hydrometeors all impact the surface downwelling longwave irradiance at times during the Arctic winter. However, none of these studies systematically investigated the contributions of each separately and in tandem with the others over an extended period of time. Moreover, as Town et al. (2005) and Doyle et al. (2011) demonstrated, evaluation of these combinations must also include the accompanying temperature and water vapor changes, which is the goal of this study. We focused our study on the single location of Utqiaġvik, Alaska, as this is one place in the Arctic where measurements are available to pursue our investigation. Choosing Utqiaġvik has the additional benefit of facilitating a comparison to prior results derived from there (e.g., Flournoy et al. 2016). Furthermore, it is near the Bering Strait, an important region of both planetary- and

synoptic-scale moisture flux into the Arctic (Newman et al. 2012) and thus represents a region important to the Arctic climate. To attribute increases in the surface downwelling longwave irradiance to specific atmospheric constituents above Utqiaġvik for the six winter seasons from 2013/14 through 2018/19, we utilized U.S. Department of Energy (DOE) Atmospheric Radiation Measurement (ARM) Program standard products generated from measurements made at its North Slope of Alaska (NSA) site located at Utqiaġvik. These products enabled us to specify vertical profiles of pressure, temperature, relative humidity, visible optical depth, and lidar circular depolarization ratio, along with lidar and radar particulate backscatter cross sections per unit volume at 1-min temporal resolution, from which we retrieved liquid- and ice-hydrometeor water contents and effective radii. Using these data as input, we ran the Rapid Radiative Transfer Model in the longwave (RRTM LW; Mlawer et al. 1997; Iacono et al. 2000) at 1-min resolution across the study period. As we will describe later, these RRTM LW computations allowed us to separate the contributions of the different atmospheric constituents to the surface downwelling longwave irradiance.

2. Methods

The study is based on three components. We first built the thermodynamic and microphysical profiles of the atmosphere over 1-min intervals using DOE ARM Program NSA site observations (Fig. 1). We subsequently imported these 1-min profiles into RRTM LW to compute the contributions to surface downwelling longwave irradiance. We then identified moisture intrusion events and performed analyses over them.

a. *Thermodynamic and microphysical states of the atmosphere*

During the study period, the DOE ARM Program launched two soundings per day, one at 0530 UTC and the other at 1730 UTC, whereas the National Weather Service launched soundings nearby at about 0023 and 1211 UTC. We linearly interpolated these four soundings of pressure, temperature, and relative humidity to 1-min temporal spacing and 20-m vertical spacing from 0 to 3 km, 50-m spacing from 3 to 4 km, 100-m spacing from 4 to 7 km, and 200-m spacing from 7 to 20 km to match the vertical layering in the DOE ARM *mergesonde1mace* product (Troyan 2012). Because of known moisture biases in soundings and sounding batch calibration errors (Turner et al. 2003, and references therein), we corrected the sounding water vapor profiles. Based on a method described in Turner et al. (2003), we used the water vapor paths retrieved from Microwave Radiometer (MWR) radiance measurements and contained in the *mwrret1liljclough* product (Turner et al. 2007b) to scale the interpolated 1-min temporal spacing relative humidity profiles so that their column-integrated water vapor matched the MWR-retrieved water vapor paths averaged to one minute. We found that this scaling reduced the errors in the computed surface downwelling longwave irradiances relative to the observed ones.

We averaged to 1-min resolution 30-m vertical resolution High Spectral Resolution Lidar (HSRL) measurements of optical depth, particulate backscatter cross section per unit volume, and circular depolarization ratio in the *hsrl* product (Eloranta 2005; Goldsmith 2016), as well as 30-m vertical resolution Ka-band ARM Zenith Pointing Radar (KAZR) measurements of radar reflectivity in the *kazrge* and *kazrmd* products (Widener et al. 2012). We subsequently interpolated the pressure, temperature, adjusted relative humidity, and KAZR radar reflectivity to the vertical grid of the HSRL, which starts near ground level (i.e., 11.25 m above the height of the HSRL on and before 12 March 2016, and 0.00 m above it afterward) and extends to approximately 20 km (i.e., 19 961.25 m above the height of the HSRL on and before 12 March 2016, and 19 980.00 m above it afterward) in 30-m steps.

Using the above measurements on the HSRL vertical grid, together with MWR-retrieved liquid-water paths in the *mwrret1liljclough* product corrected for negative and near zero ($<10\,\mathrm{g\,m^{-2}}$) amounts (e.g., Shupe and Intrieri 2004), all at 1-min intervals, we first classified liquid- and ice-dominated sample volumes within the remotely sensed vertical profiles and subsequently used them to retrieve vertical profiles of liquid- and ice-hydrometeor water contents and effective radii, as we now explain. We used HSRL particulate backscatter cross sections per unit volume that exceeded a threshold together with HSRL circular depolarization ratios that fell below a threshold to classify liquid-water dominated layers. Wang and Sassen (2001), Shupe (2007), Silber et al. (2018, their Fig. S1b), and Lamer et al. (2018) have demonstrated this classification method to be reliable. By reliable, we mean that in the two-dimensional space of backscatter cross section and circular depolarization ratio the cluster of returns identified as liquid dominated are separable from the other returns. Because of the availability of HSRL measurements of optical depth with height under all hydrometeor conditions, and the dependence of surface downwelling longwave irradiance primarily on those optical depths and temperatures up to heights to which the HSRL beam penetrated (e.g., Stephens 1978; Smith et al. 1993; Shupe and Intrieri 2004), we used HSRL measured optical depth with height as the primary constraint in all of the

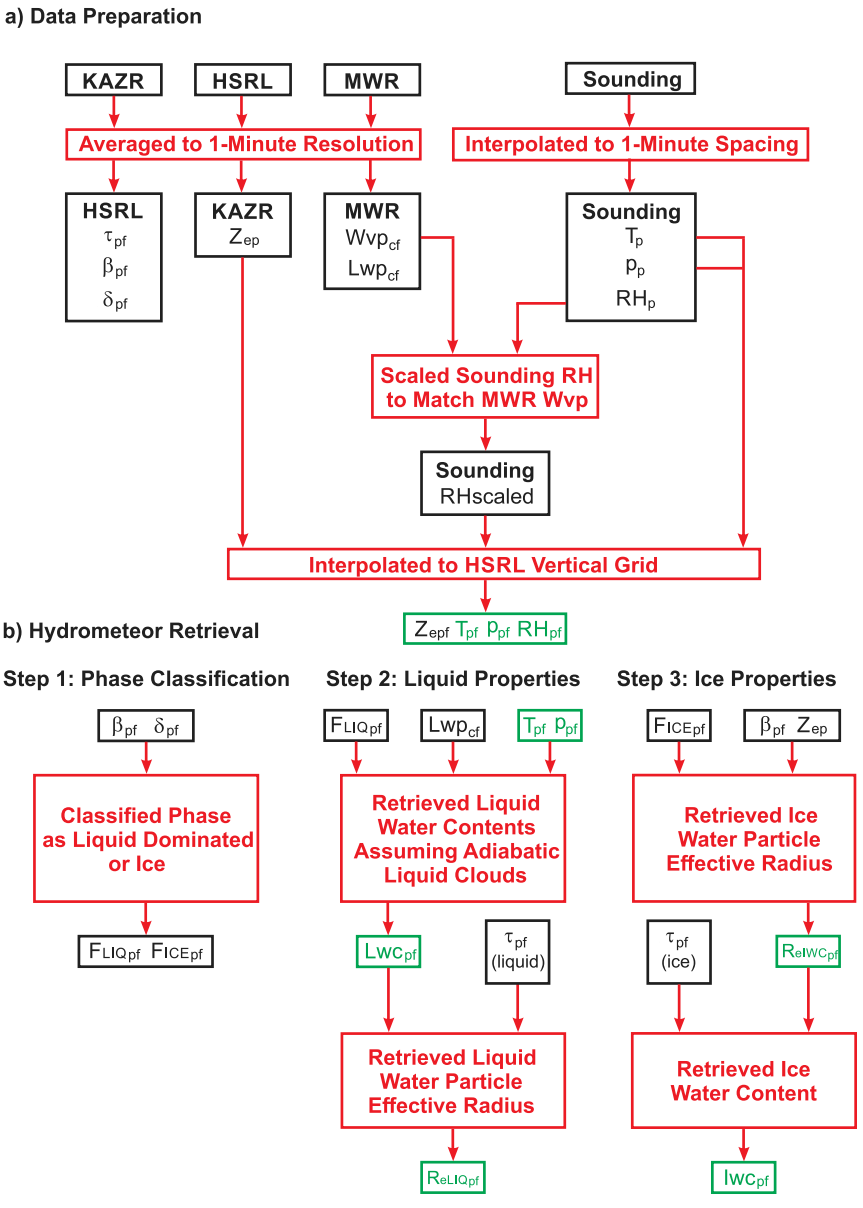

FIG. 1. Flowcharts of (a) data processing and (b) liquid- and ice-hydrometeor retrievals and products. The retrievals utilized HSRL measurements of optical depth (τ_{pf}), particulate backscatter cross section per unit volume (β_{pf}), and circular depolarization ratio (δ_{pf}), KAZR measurements of radar reflectivity (Z_{epf}), MWR measurements of water-vapor path (Wvp_{cf}) and liquid-water path (Lwp_{cf}), and soundings of temperature (T_{pf}), pressure (p_{pf}), and relative humidity (RH_{pf}). Geophysical parameters produced in the hydrometeor retrievals include a liquid-water mask (F_{LIQpf}), an ice-water mask (F_{ICEpf}), liquid-water contents (Lwc_{pf}), liquid-water particle effective radii (R_{eLIQpf}), ice-water contents (Iwc_{pf}), and ice-water particle effective radii (R_{eICEpf}). The subscript p indicates a profile of values, whereas the subscript c indicates a column-integrated amount. The subscript f represents a final product. Black boxes and geophysical parameters represent parameters not input to version 3.3 of RRTM LW, whereas green boxes and geophysical parameters represent final parameters input to version 3.3 of RRTM LW. Red arrows and boxes represent processing steps applied to the data.

hydrometeor-property retrievals. As we will show, identification of liquid and ice hydrometeors via HSRL particulate backscatter cross section per unit volume and circular depolarization ratio combined with HSRL measurements of optical depth substantially constrained the surface downwelling longwave irradiances.

Retrieval of liquid water content profiles with quantifiable accuracies is difficult, even with the instruments used in this study. As such, we assumed adiabatic liquid-water contents for each detected liquid-hydrometeor layer. If the liquid-water path calculated from these contents was greater than the MWR-retrieved liquid-water path, we multiplied all liquid-water contents by a single scale factor in order to match their sum to the MWR-retrieved value. For cases when the summed liquid-water contents were less than the MWR-retrieved value, which would happen during times when the HSRL beam attenuated before reaching an elevated liquid-water layer, we added a liquid-water content to the highest altitude 30-m layer to which the HSRL beam penetrated so as to match the MWR-retrieved value. We next calculated liquid-hydrometeor effective radii using the HSRL-measured optical depth and liquid-water content profiles, assuming that the liquid hydrometeors were in the large particle scattering limit at the HSRL wavelength. In summary, errors in liquid-water content profiles by treating them as adiabatic were offset by compensating errors in the liquid-hydrometeor effective radii so as to match the HSRL-measured optical depth. Our primary assumption here was that the HSRL-measured optical depths would best constrain the surface radiation.

We applied the ice-hydrometeor retrieval of Donovan and van Lammeran (2001) as formulated by Eloranta (2016) to all joint HSRL and KAZR returns identified as being both above the instrument-generated noise and not dominated by liquid. In this way, HSRL returns above the noise accompanied with KAZR returns in the noise were considered to be from aerosols and not processed. Visual inspection of the six years of data indicated that thin ice clouds that impacted the surface downwelling longwave irradiance and were not detected by the KAZR were rare. In the retrieval, the ratio of KAZR to HSRL particulate backscatter cross section per unit volume is used to generate a parameter called D^* that is used via a lookup table to retrieve the modal radius of a modified gamma distribution with fixed values of the parameters μ and γ (Petty and Huang 2011). Here, we generated the lookup table using spherical particles to be consistent with the use of spherical particle properties in the radiation calculations.

The one adjustment that we made to the retrieval was to decrease D^* by 75% in order to remove a bias in the computed surface downwelling longwave irradiance. After making this adjustment, we found that the surface downwelling longwave irradiances computed at 1-min intervals from ice-containing columns had similar biases and standard deviations relative to the 1-min observations as the computed irradiances for clear sky and liquid-containing columns. That a single adjustment in D^* led to similar error statistics across all years is encouraging, given that our treatment of ice particles as spheres ignores the dependence of ice-particle scattering on surface roughness across each appendage of an ice particle, the arrangement of appendages of an ice particle, the density of ice in the appendages of an ice particle, the size of the appendages in an ice particle relative to the wavelength, and the orientation of the appendages relative to the direction of incident electric fields.

The effective radius was subsequently computed from the distribution parameters and the modal radius, and the ice-water content was then computed from the HSRL optical depth and distribution parameters, treating all ice hydrometeors as spheres. Similar to the liquid-water property retrievals, the ice-water contents generated in this way compensated for errors in the effective radii retrievals so as to produce the HSRL-measured optical depths.

We used the joint HSRL and KAZR returns and the retrieved parameters based on them to create frequency of occurrence histograms of KAZR particulate backscatter cross section per unit volume, HSRL particulate backscatter cross section per unit volume, HSRL range gate optical depth, and height above the surface. We used these histograms to build a mapping from KAZR particulate backscatter cross section per unit volume to HSRL particulate backscatter cross section per unit volume and range gate optical depth that we subsequently used for the ice-hydrometeor retrievals at heights for which the HSRL beam was attenuated but the KAZR had significant detections. The only purpose of these KAZR-only retrievals was to test the sensitivity of the surface downwelling longwave irradiance to water contents at heights to which the HSRL beam did not penetrate. As we will show, the sensitivity was negligible for the purposes of this study.

b. *RRTM LW surface downwelling longwave irradiance computations over 1-min intervals*

We used version 3.3 of the RRTM LW package. We chose the RRTM solver (ISCAT = 0, i.e., absorption only) with NUMANGLES = 4. Our choices for the cloud properties were INFLAG = 2 (separate ice and liquid cloud optical depths), ICEFLAG = 2 [spherical ice particles after Key (2002) with ice-water content and ice-particle effective radius as inputs], and LIQFLAG = 1 [spherical liquid particles after Hu and Stamnes (1993) with liquid-water content and liquid-particle effective

radius as inputs]. All hydrometeor fractions in a layer were set to either 0 or 1; that is, hydrometeors detected in an instrument sample volume were assumed to be homogeneous throughout it and the failure of both instruments to detect any hydrometeors resulted in a classification of a cloud-free layer. Tang et al. (2018) demonstrated that NUMANGLES should be 2 or greater in order to reduce underestimates of about 0–4 to 0–2 $W m^{-2}$ in the surface downwelling longwave irradiance in the presence of ice clouds as a result of neglecting particle scattering in the longwave. Inspection of Fig. 4b in Kuo et al. (2017), in which both liquid and ice clouds were included, the annual mean bias in the surface downwelling longwave irradiance at Utqiaġvik was in the neighborhood of $1 W m^{-2}$ as a result of neglecting particle scattering in the longwave.

We performed the RRTM LW radiation computations across the spectral range from 3.07–1000 μm at 1-min resolution with vertical layering as follows: 200 30-m-thick layers (matched to individual HSRL sample volumes) up to approximately 6 km above ground level, 27 150-m-thick layers (matched to five HSRL sample volumes) up to approximately 10 km, 33 300-m-thick layers (matched to 10 HSRL sample volumes) up to approximately 20 km, and 48 1-km-thick layers to just under 68 km. Each layer in the computations was either completely clear (hydrometeor fraction of 0) or completely hydrometeor filled (hydrometeor fraction of 1). For heights below 20 km, we set temperature, water vapor amount, liquid-water amount, and ice-water amount to the values in our datasets. At these altitudes, we set the five major radiatively active gaseous constituents O_3, N_2O, CO, CH_4, and O_2 to the values in RRTM LW atmospheric profile 5 (i.e., "subarctic winter model") while we set CO_2 to 397.5 ppmv. Above 20 km, we set all properties to values in the RRTM LW subarctic winter model but with CO_2 again set to 397.5 ppmv. We then ran RRTM LW with different combinations of constituents—dry gas, water vapor, liquid hydrometeors, and ice hydrometeors—at 1-min resolution to determine their contributions to the surface downwelling longwave irradiance. We chose the properties of spheres for the RRTM LW computations. We compared the RRTM LW computed surface downwelling longwave irradiances to Eppley Laboratory, Inc., Precision Infrared Radiometer (PIR; spectral response from 3.5 to 50 μm) measurements contained in the DOE ARM Program *skyrad60s* product.

The *skyrad60s* irradiance product contains two 1-min averaged surface downwelling longwave irradiance measurements for every minute. Over the usable 1 360 522 (of 1 565 280) 1-min samples in the study period, these two sets of measurements had a mean difference of $0.27 W m^{-2}$ and a root-mean-square difference of $1.33 W m^{-2}$; we used the averages of these two 1-min measurements in the comparisons that follow. Gröbner et al. (2014) demonstrated that current calibration methods for the PIR have most likely resulted in an $\sim 5 W m^{-2}$ low bias in its measurements. However, this low bias linearly decreases in magnitude as the atmospheric water vapor path decreases from 10 to 0 mm (a range of values typical of wintertime conditions on the NSA), leaving a final bias of only 1–2 $W m^{-2}$. Given these bias properties, together with calibration uncertainties of $\pm 4 W m^{-2}$ reported by Andreas et al. (2018) and Reda et al. (2012), RRTM LW computations that agree with the PIR measurements to approximately $\pm 4 W m^{-2}$ are the best that we expect, with errors in atmospheric state parameters input into the RRTM LW computations leading to even larger errors.

In summary, the retrieval framework used for this study required nominal quality soundings, HSRL, KAZR, and MWR data products. In addition, evaluation of the quality of the RRTM LW computations based on these soundings and data products required calibrated surface downwelling longwave irradiance measurements contained in the *skyrad60s* product. These requirements limited us to a study period from 1 November 2013 to 30 April 2019, with a significant loss of sufficient quality HSRL data from 20 January to 30 April 2018. The methodological approach here is similar to the previous studies by Dong et al. (2010) and Shupe et al. (2015). Our approach is most similar to Shupe et al. (2015) with primary differences being that they used infrared spectral radiance measurements to retrieve cloud optical depths of thinner liquid clouds, whereas we used the optical depths measured by a HSRL to characterize thinner hydrometeor optical depths. We also used a different approach to retrieve ice-particle properties, and the use of radiative closure here was to assess the impacts of the different constituents on the surface downwelling longwave irradiance.

c. *Identification of moisture intrusion events*

To identify moisture intrusion events, we averaged the 1-min temporal resolution data from ARM to daily values for the six months from November through April for the six winter seasons of 2013/14 through 2018/19. This produced a time series of 1087 days in length. We assigned missing values to 112 days when retrievals were not available. This included a large stretch of 101 days between 20 January and 30 April 2018.

We computed anomalous daily values of each variable (see the caption of Fig. 9 for a list of the variables included in the analysis) by subtracting from each daily value its smoothed calendar-day climatology. To find the smoothed calendar-day climatology, we first found the raw calendar-day climatology by averaging the daily values across the six seasons. This resulted in a rather

noisy, 182-day length time series extending from 1 November to 30 April for each variable. Despite the noise, a distinct seasonal cycle was embedded in each variable's time series. We extracted this seasonal cycle, and hence the smoothed calendar-day climatology, by fitting a second-order polynomial to the raw calendar-day climatology. Visual inspection of the smoothed calendar-day climatology for each variable revealed a reasonable fit, further supported by the net anomalous daily values being close to zero for each variable when summed across all 1087 days.

In addition to constructing anomalous daily values for each variable individually, we also calculated anomalous daily values of total column water (TCW) to identify warm, moist intrusion events. Because of the physics underlying the Clausius–Clapeyron relationship, the identification of warm, moist intrusions via TCW would also identify periods of elevated temperatures. Daily values of total TCW were first found by summing the daily averaged values of water vapor, liquid, and ice water paths, with water vapor being the dominant constituent. Anomalous daily values of TCW were then found in the same manner used for the individual variables.

Having found the anomalous daily values of each variable, we composited them against TCW intrusion events. We preliminarily identified the TCW intrusion events by selecting days from the anomalous TCW time series that exceeded two standard deviations. We then trimmed the preliminary selection by only retaining the events with the highest anomalous TCW within any 14-day time period. This helped to ensure independence among the events. Furthermore, we did not include events that fell before 16 November or after 15 April in order to minimize the number of missing values for events that fell on the flank of a particular season. The final number of events included in the composites was 15. We centered these 15 events into a composite at lag day 0, defined as the day within the TCW intrusion that the TCW attained its maximum value. The composites were extended from lag day −20, before the event occurred, to lag day +20, after the event occurred. Our goal with these composites was to examine the temporal evolution of each variable during the TCW intrusions along with estimating the typical time scale over which these events occurred. We determined significance for the composites using a Student's t test. The null hypothesis that we sought to reject was that the composited mean for each variable was not significantly different from its mean calculated across the entire 1087-day time series. Before plotting, we normalized the lagged composites by each variable's respective standard deviation.

As we will show in section 3b, the typical time scale of the events extended from 10 days prior to the peak TCW anomaly to 5 days afterward, for a total period of 15 days. However, there was variability in the time series that did not always match the average time window of 15 days. Because of this variability, we searched in the environs of the beginning and ending day of each intrusion event for a minimum in the water vapor path, a zero liquid-water path, a zero ice-water path, and, as a result, a resulting minimum in the surface downwelling longwave irradiance. We adjusted each event window to the starting and ending times that we identified in this way. All of the intrusion events started and ended during clear-sky periods with little variation in properties. The final event windows that we arrived at for all 15 events are illustrated by boxes in many of the figures.

3. Results

To illustrate the thermodynamic nature of the six winter seasons from 2013/14 through 2018/19 at Utqiaġvik, we first present height versus time plots of atmospheric temperature and water vapor mixing ratio in Figs. 2 and 3, respectively, obtained from all of the DOE ARM NSA site radiosondes launched during the study period. As Figs. 2 and 3 show, there were many intrusions of air with enhanced temperature and absolute humidity into the Utqiaġvik region during each winter, with values approaching approximately 10°C and 4 g m^{-3}, respectively. The degree to which these intrusions and their associated surface downwelling longwave irradiances were anomalous in nature will be examined in section 3b.

The results to follow for the six winter seasons at Utqiaġvik are grouped into three sections. The first section contains summary results for all of the six winter seasons. In the second section, we follow the analysis method described in Doyle et al. (2011) to characterize the impact of liquid- and ice-water hydrometeors, in addition to water vapor and temperature, on the surface downwelling longwave irradiance during intrusions of warm, moist air. In the last section, we present our results in the context of those of Flournoy et al. (2016), whose study motivated us to assess the impacts of ice hydrometeors throughout a vertical column on the surface downwelling longwave irradiance.

a. Contributions by temperature, water vapor, liquid-, and ice-water to surface downwelling longwave irradiance

For illustrative purposes we present in Fig. 4 daily averages of the temperature profiles (Fig. 4a), water vapor content profiles (Fig. 4b), optical depths measured by the HSRL for liquid-water hydrometeors (Fig. 4c) and ice-water hydrometeors (Fig. 4d), column-integrated optical depths of the liquid- and ice-water hydrometeors (Fig. 4e),

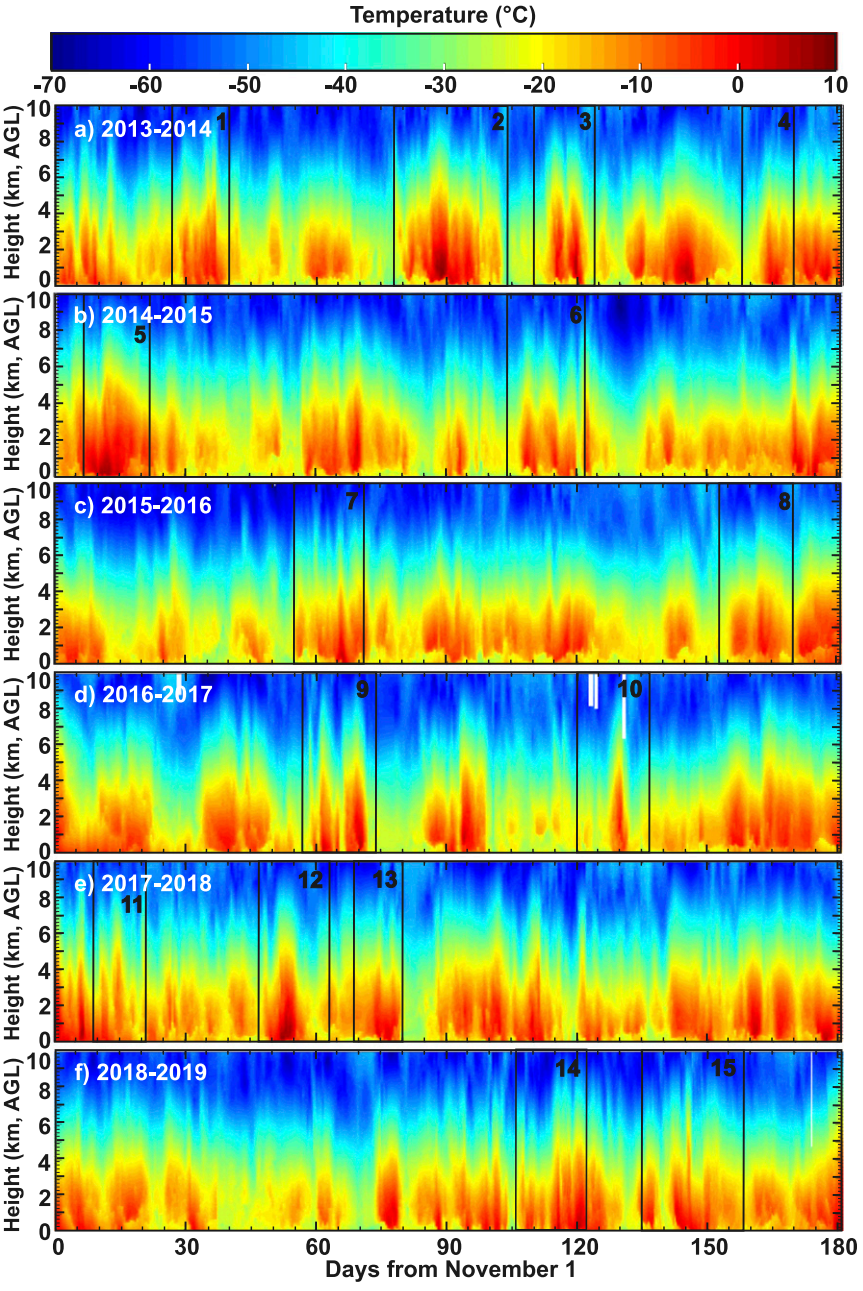

FIG. 2. Contour plots of vertical profiles of temperature (in °C) obtained from twice daily DOE ARM NSA site radiosondes for the six winter seasons from 2013/14 through 2018/19. The black boxes indicate the 15 intrusions of warm, moist air analyzed in the study.

and column-integrated water vapor, liquid, and ice paths (Fig. 4f) for the 2013/14 winter season. (Corresponding illustrations of the information in Figs. 4c–f for all six winter seasons are contained in Fig. S1 in the online supplemental material through Fig. S4). The daily averaged liquid-hydrometeor optical depths (Fig. 4c) were confined to a smaller range of heights relative to the daily averaged ice-hydrometeor optical depths (Fig. 4d). Because the height of liquid-water layers within a day varied considerably, the daily averaged liquid-water optical depths were vertically spread out much more than their 1-min counterparts, which most often occurred in geometrically thin (less than a few hundred meters) layers (not shown). The ice hydrometeors were deep during the intrusion events, often reaching altitudes of 8 km or higher (Fig. 4d). The ice-hydrometeor optical depths over 30-m vertically thick layers were smaller than those for liquid water (cf. the darker reds in

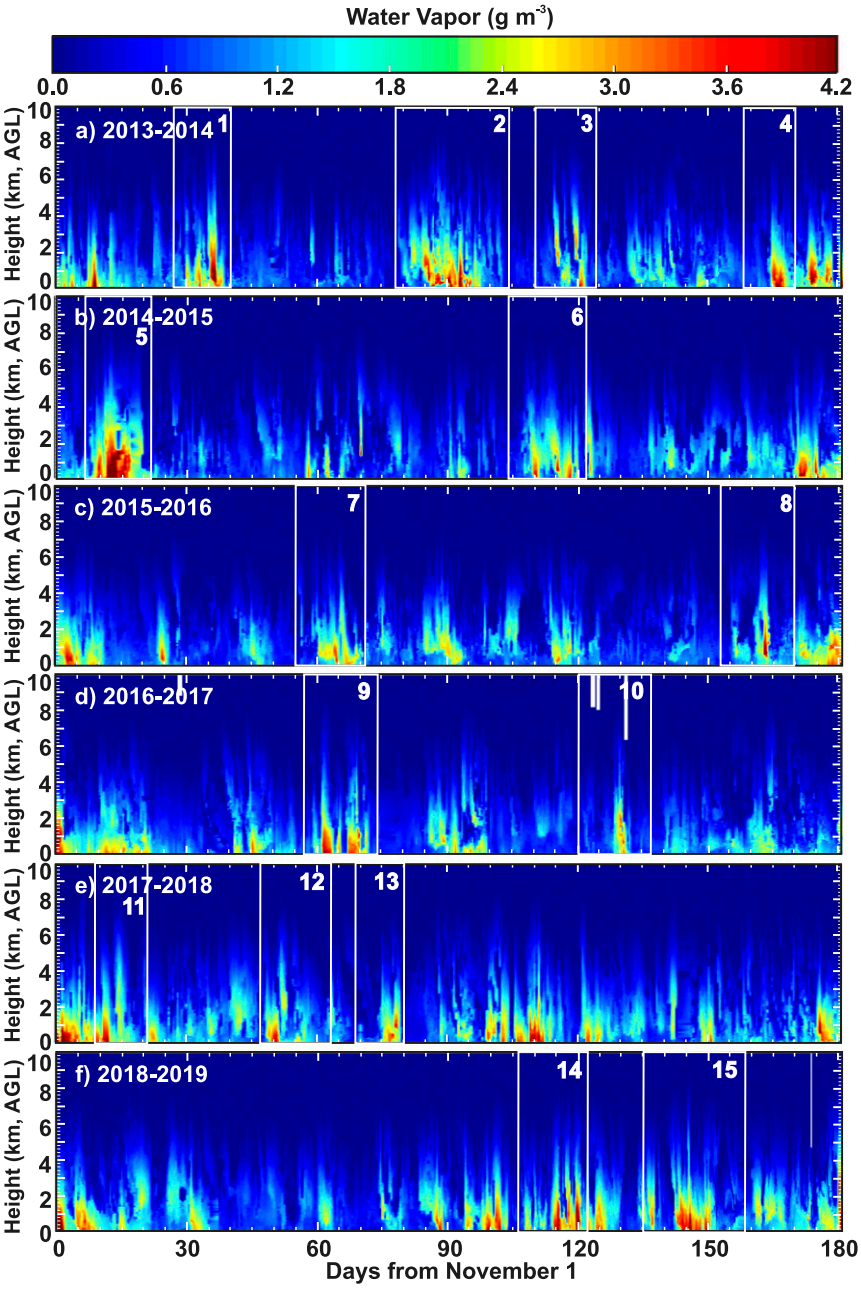

FIG. 3. Contour plots of vertical profiles of water vapor content (in g m^{-3}) obtained from twice daily DOE ARM NSA site radiosondes for the six winter seasons from 2013/14 through 2018/19. The white boxes indicate the 15 intrusions of warm, moist air analyzed in the study.

Fig. 4c to the lighter reds in Fig. 4d). As the averaged liquid- and ice-water column optical depths measured by the HSRL indicate in Fig. 4e, liquid- and ice-hydrometeor optical depths were, at times (e.g., days 10–14, days 36–39, days 52–53, and days 79–88), comparable in magnitude, in agreement with Curry and Ebert (1992) and Shupe and Intrieri (2004). At other times, they were both optically thin. This finding requires that both liquid and ice hydrometeors be included in the radiative transfer calculation to most accurately estimate the surface downwelling longwave irradiance for all days. The total optical depth in Fig. 4e (represented by the black line) illustrates the total optical depth as a result of adding to the liquid-water optical depth any ice-water optical depth that occurred at the same time. The contributions of the ice hydrometeors to the optical depths of the liquid

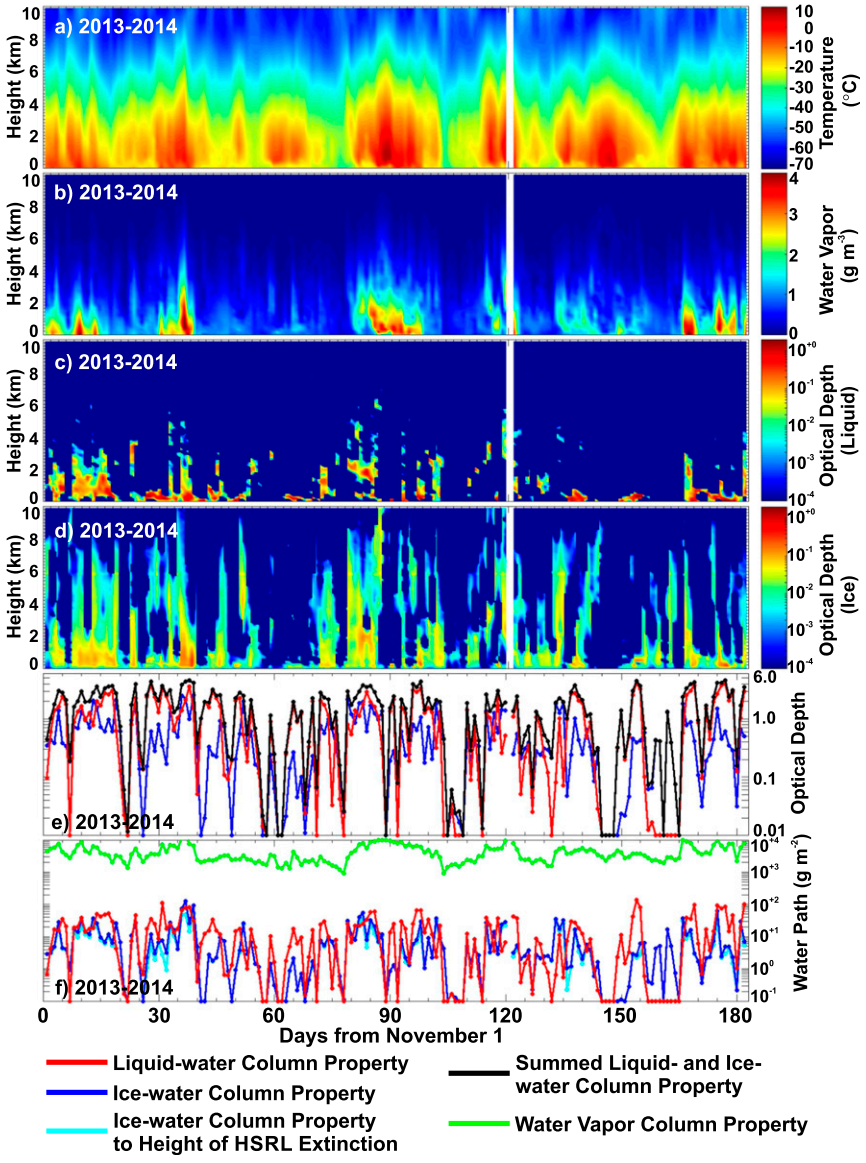

FIG. 4. Daily averaged vertical profiles of (a) temperature (in °C) and (b) water vapor mixing ratio (in g m^{-3}) obtained from twice daily DOE ARM NSA site radiosondes. Daily averaged (c) liquid-water optical depths and (d) ice-water optical depths over 150-m vertically thick layers obtained from the 30-m resolution HSRL measurements. (e) Column integrated values of the liquid-water optical depths in (c) (red line) and ice-water optical depths in (d) (blue line), as well as their sum (black line). The daily averaged optical depths in (c) and (d) include both clear and cloudy/precipitating periods. (f) Column integrated values of daily averages of retrieved liquid-water content (red line), ice-water content up to the height of HSRL extinction (cyan line), ice-water content to the top of the column (blue line), and water vapor path (green line). All panels are for the 181-day period composing the 2013/14 winter season.

hydrometeors were often significant in that the surface downwelling longwave irradiances were sensitive to these contributions for the range of optical depths that occurred over the six winter seasons (Fig. 5). The daily averaged column liquid- and ice-water path amounts are shown in Fig. 4f. The combined water-path amounts were often around 20 g m^{-2} or less, values to which the surface downwelling longwave irradiance is sensitive (Turner et al. 2007a).

The average of the surface downwelling longwave irradiance over the usable 257 703 (of 260 640 possible) 1-min RRTM LW computations during the 181-day 2013/14 winter season was 204.0 W m^{-2} based on all constituents (Table 1, row 2 and column DryVLI) and

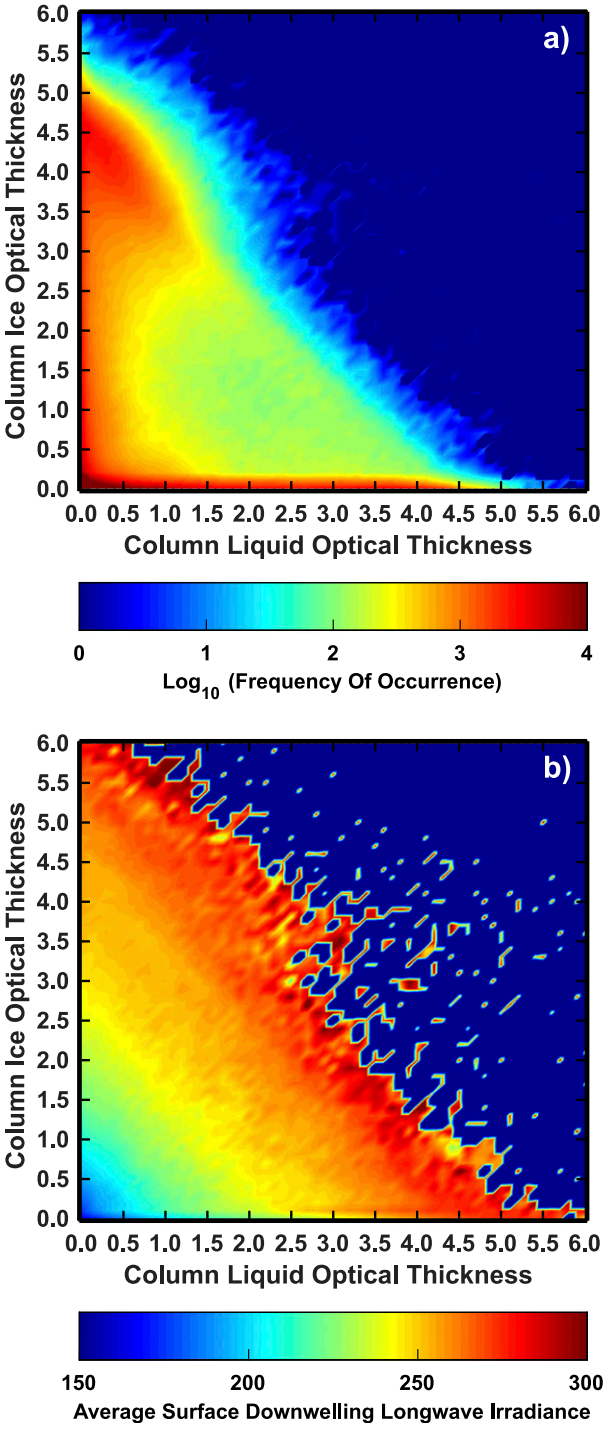

FIG. 5. (a) Frequency of occurrence histogram of HSRL measured column liquid- and ice-optical thicknesses. The color in each 0.1 by 0.1 bin represents the number of occurrences over the six winter seasons of the joint column liquid- and ice-optical thicknesses corresponding to that bin. (b) Average of the surface downwelling longwave irradiances over the occurrences illustrated in (a). Note that few total optical thicknesses greater than five were obtained from the HSRL measurements and ice hydrometeors with optical thicknesses less than 0.2 below boundary layer liquid-water clouds were a frequent occurrence.

203.8 W m^{-2} for the observations (Table 1, row 2 and column Obs). Over the entire six years, the average over the useable 1 360 522 (of 1 565 280 possible) 1-min resolution samples was 205.0 W m^{-2} for the RRTM LW computed surface irradiances, whereas the average of the observed surface irradiances was 206.7 W m^{-2} (Table 1, row 1). The root-mean-square difference between the computed and observed 1-min irradiances for the 2013/14 winter season was 5.38 W m^{-2}, whereas across the entire study period it was 5.83 W m^{-2}. Inspection of Table 1 indicates that over the last four years of the study period a consistent bias emerged between the computed and observed irradiances, attaining a value of −3.3 W m^{-2} for the 2018/19 winter season, with the minus sign indicating that the computed irradiances were too low. (We have evidence that at least part of the bias was a result of MWR-retrieved water vapor paths being slightly too low for the computed irradiances to match the observed irradiances.)

A time series of the daily averaged RRTM LW computations (in gold) and observations (in black) for the 2013/14 winter season are provided in Fig. 6a (the black line is mostly obscured by the gold line). The bias that developed in the last four years of the study period is evident by the gold and black lines slowly diverging in Fig. 6c through Fig. 6f.

We separated the 1 360 522 usable 1-min temporal resolution atmospheric columns in the study into clear sky columns (117 353 samples), liquid-water only columns (19 580 samples), ice-water only columns (540 523 samples), and liquid- and ice-water containing columns (683 066 samples) and compared the computations for each to their measured values. This led to mean and root-mean-square differences of −2.88 and 3.88 W m^{-2} for clear-sky columns, −3.52 and 6.89 W m^{-2} for liquid-only columns, −1.79 and 5.22 W m^{-2} for ice-only columns, and −1.22 and 6.45 W m^{-2} for liquid- and ice-containing columns. These differences are comparable to each other, indicating that no one type of column dominated the overall errors. One possible contributor to all of the errors was the development of a dry bias in the MWR-retrieved water vapor paths in the last four years of the study. Another possible contributor to the larger bias for liquid hydrometeors is that they sometimes occurred too close to the HSRL for the HSRL to provide usable measurements of them. At these times the HSRL would report an incomplete optical depth profile because of the unsampled hydrometeors close to it, leading to an underestimate of the liquid-hydrometeor optical depth, hence to an underestimate of the surface downwelling longwave irradiance.

Encouraged by this level of agreement between the computed and measured surface downwelling longwave irradiances, we evaluated contributions from individual constituents to the RRTM LW computed surface downwelling longwave irradiances. Over the six winter seasons,

TABLE 1. Surface downwelling longwave irradiances averaged over all months, years, and the entire 6-yr period for the observations (Obs) and RRTM LW computations for dry gas (Dry), dry gas and liquid water (DryL), dry gas and ice water (DryI), dry gas, liquid water, and ice water (DryLI), dry gas and water vapor (DryV), dry gas, water vapor, and liquid water (DryVL), dry gas, water vapor, and ice water (DryVI), and dry gas, water vapor, liquid water, and ice water (DryVLI).

	Obs	Dry	DryL	DryI	DryLI	DryV	DryVL	DryVI	DryVLI
All six seasons	206.7	71.9	132.2	113.1	153.1	172.0	195.8	189.8	205.0
2013/14	203.8	72.0	131.6	111.5	150.6	172.4	195.5	189.4	204.0
Nov	219.3	73.0	145.7	123.9	168.2	179.1	208.3	201.3	218.6
Dec	203.0	70.8	135.2	113.9	155.2	168.6	194.2	186.6	202.9
Jan	196.3	70.2	126.2	108.0	145.0	166.0	187.5	182.4	195.9
Feb	194.9	70.9	120.1	109.5	140.2	167.5	186.3	184.2	195.2
Mar	192.9	72.8	111.6	98.9	127.7	171.5	186.6	183.4	194.1
Apr	216.0	74.4	150.7	114.9	166.8	181.6	210.2	198.7	217.4
2014/15	201.4	71.5	124.4	113.6	147.9	170.5	191.2	188.8	201.6
Nov	227.4	78.8	155.9	111.4	167.1	193.2	221.7	206.2	226.3
Dec	193.3	68.0	127.8	107.9	146.7	158.3	183.7	177.1	192.6
Jan	184.9	70.0	99.1	108.9	124.3	161.1	173.1	178.7	184.7
Feb	198.5	69.7	118.7	124.0	150.4	166.6	185.1	189.1	198.6
Mar	184.3	67.1	99.0	111.3	132.4	159.2	171.5	178.9	186.7
Apr	219.5	75.1	145.7	118.5	166.6	183.4	211.1	202.0	220.2
2015/16	201.0	70.4	131.9	105.5	147.7	167.1	191.6	182.6	198.8
Nov	217.2	71.2	149.3	124.4	170.2	175.0	205.5	198.0	215.1
Dec	184.3	64.8	118.6	100.1	137.3	149.7	173.4	167.1	182.8
Jan	215.3	72.0	149.6	116.0	169.2	175.1	204.9	193.2	213.0
Feb	197.0	71.2	124.4	101.4	139.3	167.0	187.5	180.1	194.1
Mar	176.7	68.2	105.5	84.3	112.4	155.1	171.0	162.9	174.4
Apr	217.1	76.0	145.4	107.2	158.4	182.9	209.4	195.7	214.8
2016/17	203.8	71.6	127.5	106.4	144.8	170.7	193.2	186.3	201.2
Nov	245.9	76.0	198.3	122.9	207.0	189.9	238.9	210.7	243.2
Dec	203.5	71.2	130.6	105.4	146.2	167.7	192.5	183.5	200.0
Jan	200.5	69.7	117.5	110.7	142.4	169.3	187.1	187.2	198.4
Feb	196.3	68.4	114.4	117.8	147.5	161.3	180.7	183.5	195.6
Mar	179.5	68.0	93.0	97.0	112.2	158.8	168.6	171.8	177.6
Apr	200.4	76.5	117.3	86.9	120.0	178.0	194.6	182.9	195.9
2017/18	232.0	75.4	155.6	134.9	186.7	184.1	216.5	208.9	229.3
Nov	254.7	78.3	178.6	153.2	215.7	196.7	236.5	226.9	251.4
Dec	225.6	74.1	140.8	135.7	179.4	180.0	207.1	206.1	223.2
Jan	205.7	72.9	143.5	102.7	151.2	170.7	199.9	183.8	203.2
Feb									
Mar									
Apr									
2018/19	212.1	72.1	135.0	119.1	159.5	173.7	198.2	193.6	208.8
Nov	234.3	74.4	176.7	133.1	197.2	182.2	222.8	206.6	231.5
Dec	198.5	67.0	128.8	119.4	158.2	155.7	182.1	179.9	195.9
Jan	187.8	68.2	111.1	99.4	128.3	159.3	176.2	173.0	184.0
Feb	218.3	74.2	122.7	128.9	159.3	181.8	199.7	203.7	214.8
Mar	225.0	74.4	141.5	129.7	171.6	184.6	209.0	207.0	221.7
Apr	211.4	75.0	131.7	105.9	145.4	180.6	201.9	193.5	207.8

incorporating only dry gases yielded an average value of 71.9 $W m^{-2}$ (Table 1, column Dry) with daily averaged values ranging between 50 and 100 $W m^{-2}$ (Fig. 7, lower black line in each panel). Figure 7 also illustrates the daily averaged results of the RRTM LW computations for the dry gases and water vapor (green lines), the dry gases and liquid hydrometeors (red lines), and the dry gases and ice hydrometeors (blue lines). The spectral content of the surface downwelling longwave irradiance from water vapor is not the same as that from liquid- and ice-water particles. In the dry Arctic winter atmospheres of our study, water vapor was optically thick at some wavelengths (e.g., within its rotation and vibration-rotation bands) and optically thin at others (e.g., 8–12 μm), whereas liquid- and ice-water hydrometeors were at times not optically thick at any wavelength and at other times close to optically thick across the infrared. As a result, combining these constituents together did not always lead to a linear response in surface downwelling longwave irradiance, as illustrated by Fig. 7. The computed irradiances minus the observed

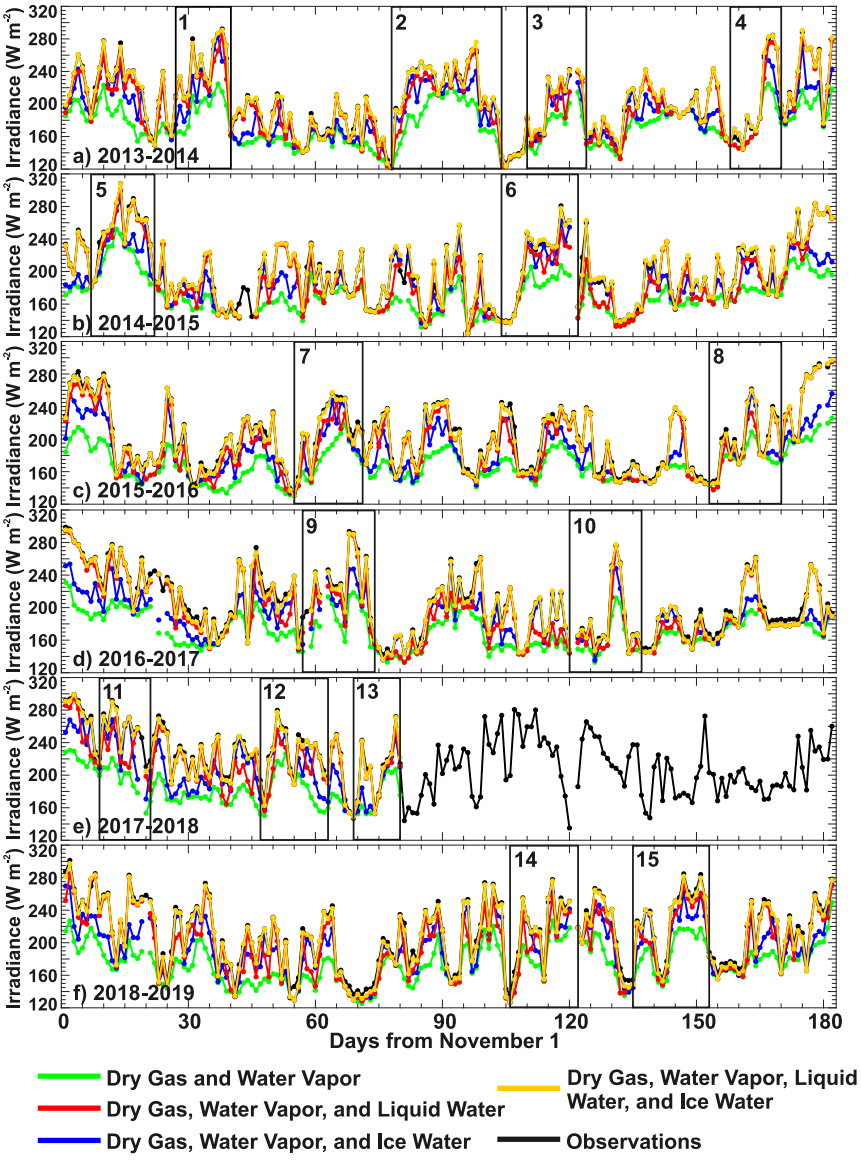

FIG. 6. Daily averaged surface downwelling longwave irradiances obtained from dry gas and water vapor (green line), dry gas, water vapor, and liquid water (red line), dry gas, water vapor, and ice water (blue line), dry gas, water vapor, liquid water, and ice water (gold line), and the observations (black line). These data cover all six winter seasons, illustrating the period of missing HSRL data in the second half of the 2017/18 winter season. The black boxes indicate the 15 intrusions of warm, moist air analyzed in the study.

irradiances, averaged over the analysis period, are $-34.7\,\mathrm{W\,m^{-2}}$ for the dry gases and water vapor, $-74.5\,\mathrm{W\,m^{-2}}$ for the dry gases and liquid hydrometeors, and $-93.6\,\mathrm{W\,m^{-2}}$ for the dry gases and ice hydrometeors. When liquid hydrometeors (Fig. 6, red lines) or ice hydrometeors (Fig. 6, blue lines) were separately added to water vapor, their RRTM LW values differed from the observed values on average by -10.9 and $-16.9\,\mathrm{W\,m^{-2}}$. Repeating the calculation with the combination of dry gases, liquid, and ice hydrometeors, we found the deviation from the observations to be $-53.6\,\mathrm{W\,m^{-2}}$ (Fig. 7, gold lines). These results indicate that during the analysis period water vapor was by far the single most important constituent, with the contributions by liquid and ice being comparable.

Table 1 contains summary statistics of the results described in section 3a further broken down by year and month within each year. Most months have greater contributions from adding liquid hydrometeors to the vapor (Table 1, column DryVL) than adding ice hydrometeors to the vapor (Table 1, column DryVI),

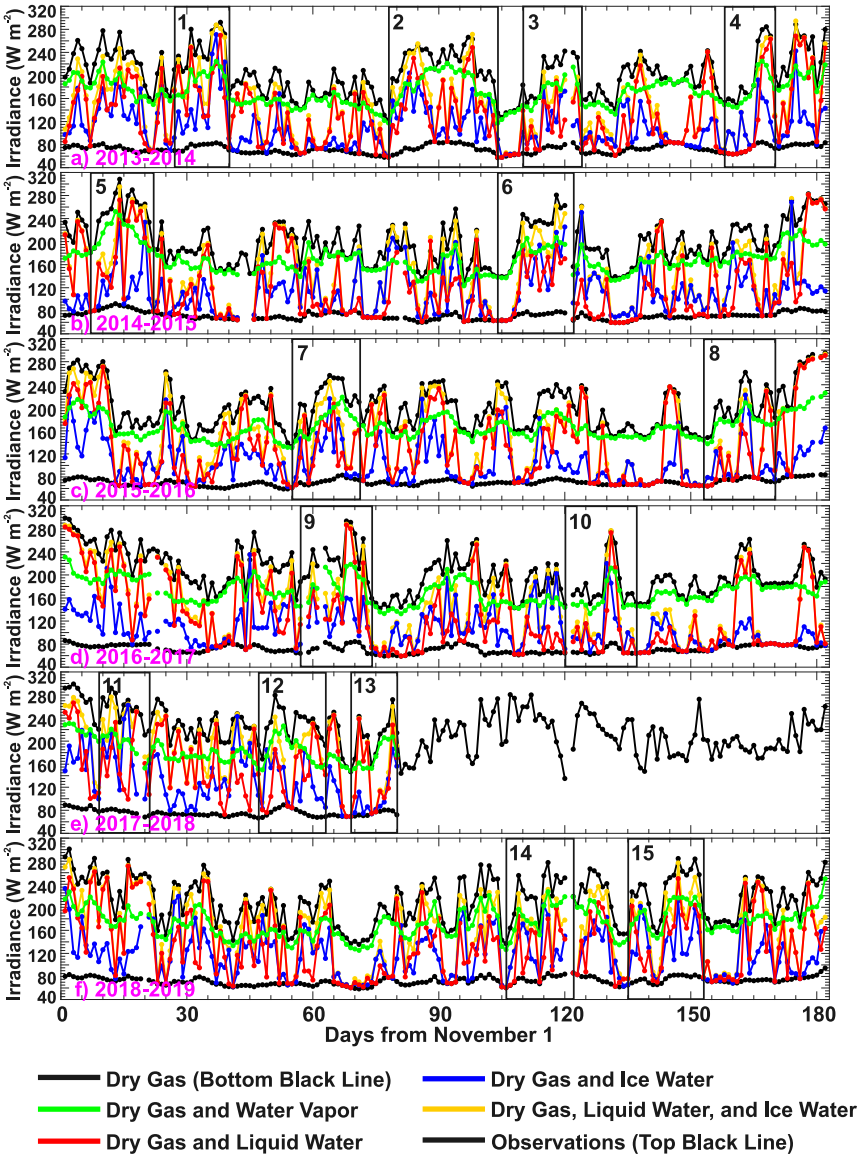

FIG. 7. Daily averaged surface downwelling longwave irradiances obtained from dry gas (bottom black line), dry gas and water vapor (green line), dry gas and liquid water (red line), dry gas and ice water (blue line), dry gas, liquid water, and ice water (gold line), and the observations (top black line). These data cover all six winter seasons, illustrating the period of missing HSRL data in the second half of the 2017/18 winter season. The black boxes indicate the 15 intrusions of warm, moist air analyzed in the study.

although this reverses at times in the months of January, February, and March.

b. *Changes in surface irradiance caused by moisture intrusion events*

To estimate the increase in the surface downwelling longwave irradiances as a result of moisture intrusion events, we first identified the intrusion events and a baseline irradiance for each of the events. Using the procedure outlined in the methods, we computed anomalous daily values of TCW (Fig. 8) and applied the two-standard deviation threshold (Fig. 8, horizontal dashed lines). Fifteen periods passed the threshold test (Fig. 8, vertical dashed lines) while also meeting our other criteria outlined in the methods. We computed anomalous daily values for the retrieved water variables, observed surface downwelling longwave irradiances, and RRTM LW computed surface irradiances with different combinations of constituents. Compositing these anomalies over a 40-day window centered on the maximum TCW anomaly for

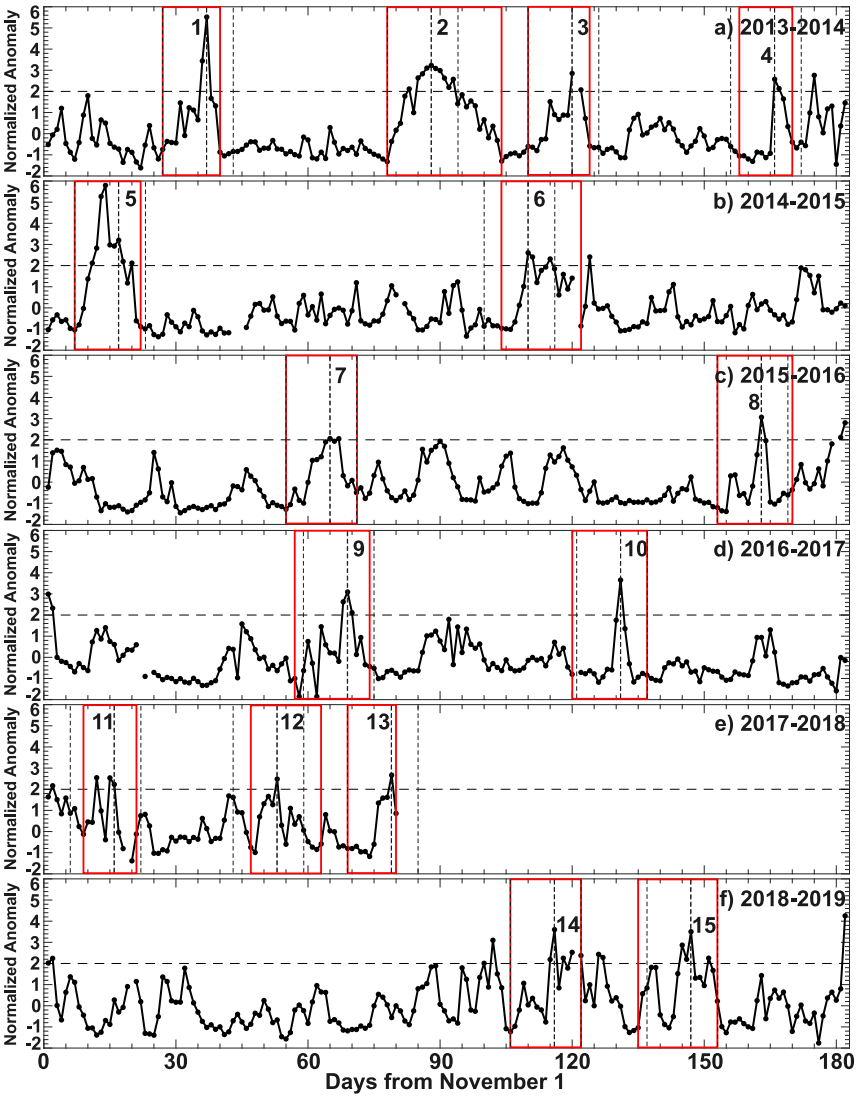

FIG. 8. Daily total (i.e., water vapor, liquid water, and ice water) column water (TCW) anomalies, together with the two standard deviation threshold (horizontal dashed lines). The groups of three vertical dashed lines represent the average beginning, center, and ending times of the 15 intrusion events investigated in this study. The solid red boxes represent the intrusion events after accounting for variability from event to event.

an event led to the results illustrated in both panels of Fig. 9.

Inspection of the results in Fig. 9 led us to define an event as corresponding to the time period extending from 10 days prior to the peak TCW anomaly to 5 days afterward. Our choice for this range was motivated by the occurrence of some statistically significant negative values 10 days prior to the peak of an event followed by the loss in significance for most variables after about 5 days after the event. We identified in Fig. 8 the locations of these 15-day periods for all 15 intrusion events by the groups of three vertically dashed lines per event. As Figs. 6–8 illustrate, there was variability in the time series that did not always match the average time window of 15 days. Because of this variability, we adjusted the beginning and ending times according to the procedure described in section 2b. We chose the properties at the first time in each event to serve as the baseline.

For illustrative purposes, consider intrusion event 2. A hydrometeor-free period occurred at 0600 UTC on day 78, near the beginning of the 10-day (on average) window running up to the peak of the event (Fig. 8, row 1). The observed surface downwelling longwave irradiance at the beginning of the event was 117.7 $\mathrm{W\,m^{-2}}$ (Fig. 6, row 1).

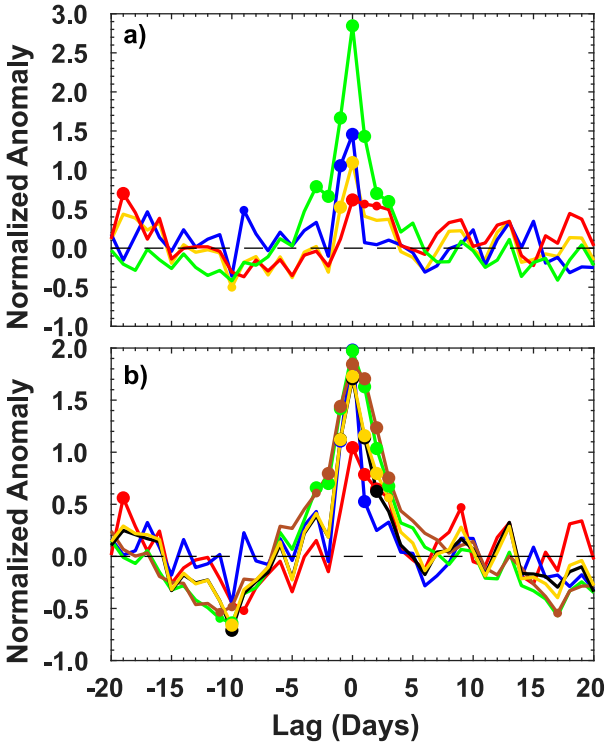

FIG. 9. (a) Lag composites of the liquid optical depths (red line), ice optical depths (blue line), total optical depths (gold line), and total column water (green line). (b) Lag composites of the surface downwelling longwave irradiances based on the observations (black line), as well as the RRTM LW computations for the dry gas (brown line), dry gas and water vapor (green line), dry gas and liquid water (red line), dry gas and ice water (blue line), and dry gas, water vapor, liquid water, and ice water (gold line). The large solid circles represent significance at the 95% level, whereas the small solid circles represent significance at the 90% level.

The mean value of the observed irradiance over the 15-min window to follow was 117.8 W m^{-2} with a standard deviation of 0.05 W m^{-2}, attesting to little variation of the properties at the start of this intrusion. The time of the end of event 2 was not clear, so we chose 2300 UTC on day 104 because of the clear minima in water vapor and observed irradiances at this time.

Again, using event 2 for illustrative purposes, we estimated the fractional change in the surface irradiance, relative to the baseline time, that resulted from temperature changes of dry gas only. The baseline RRTM LW irradiance from the dry gas was found to be 57 W m^{-2} (Fig. 10, gray dot in subcolumn 1 for event 2; Table 2 summarizes the event 2 results to follow in the E2 section of the table), while the average RRTM LW computed surface irradiance from the dry gas with temperature varying during the intrusion event was 74 W m^{-2} (Fig. 10, black dot in subcolumn 1 for event 2), representing an average fractional increase of 1.30 as a result of increased temperatures during the intrusion.

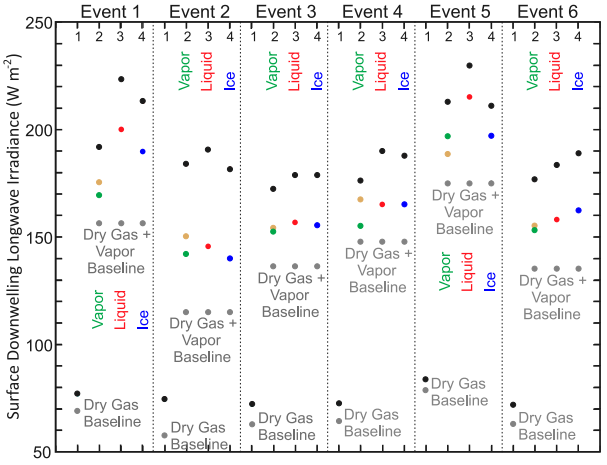

FIG. 10. Results of the analysis for the first six intrusion events. The baseline irradiances for the dry gas are indicated by the lower gray dots, whereas those for the dry gas together with water vapor are represented by the upper gray dots. The black dots just above the dry gas baseline values represent the increase in the surface downwelling longwave irradiance that resulted from temperature increases of the dry gas during the intrusion event. The vertical distance between the dry gas and dry gas plus water vapor baselines (i.e., the gray dots within an intrusion event) represents the increase in surface downwelling longwave irradiance as a result of adding the baseline amount of water vapor to the baseline amount of dry gas for the intrusion event. The gold dots indicate the average surface downwelling longwave irradiance over the intrusion event as a result of temperature changes above their baseline value with water vapor and pressure fixed to their baseline values. The green, red, and blue dots indicate the average surface downwelling longwave irradiance over the intrusion event as a result of water vapor, liquid water, or ice water changes, respectively, above their baseline dry gas plus water vapor values with pressure and temperature held fixed. The black dots indicate the average surface downwelling longwave irradiance over the intrusion event as a result of temperature and either water vapor, liquid water, or ice water changes above their baseline dry gas plus water vapor values with now only pressure held fixed. The vertical distances from the gray dots representing the dry gas plus water vapor baseline to the green, red, and blue dots for each constituent represent the efficacy of the constituent alone in elevating the surface downwelling longwave irradiance above its baseline value during the intrusion event. The vertical distances from the green, red, and blue dots to the black dots above them represent the additional increase in surface downwelling longwave irradiance from a constituent as a result of both constituent and temperature changes during the intrusion event. These results are presented in tabular format within Table 2 for all 15 intrusion events.

We added the water vapor to dry air at the baseline time and computed an irradiance of 115 W m^{-2} (Fig. 10, gray dots in subcolumns 2–4 for event 2). Following Doyle et al. (2011), we first held the vapor fixed across the intrusion event while allowing temperature to vary, which led to an average RRTM LW computed irradiance across the event of 150 W m^{-2} (Fig. 10, gold dot in subcolumn 2 for event 2), an increase of 35 W m^{-2} over

TABLE 2. Summary table of the results illustrated in Fig. 10, but for all 15 intrusion events.

	Air	Vapor	Liquid	Ice	Air	Vapor	Liquid	Ice	Air	Vapor	Liquid	Ice
Content + temperature	E1	192	223	213	E2	184	191	182	E3	172	179	179
Temperature		176				150				154		
Content		169	200	190		142	145	140		152	157	156
Dry gas + vapor base		156	156	156		115	115	115		136	136	136
Temperature	76				74				71			
Dry gas base	69				57				63			
Content + temperature	E4	176	190	188	E5	213	230	211	E6	177	183	189
Temperature		168				189				155		
Content		155	165	165		197	215	197		153	158	163
Dry gas + vapor base		148	148	148		175	175	175		135	135	135
Temperature	72				83				72			
Dry gas base	64				79				63			
Content + temperature	E7	178	180	175	E8	175	183	181	E9	184	211	191
Temperature		147				165				166		
Content		150	153	148		150	157	154		160	182	166
Dry gas + vapor base		123	123	123		141	141	141		145	145	145
Temperature	73				74				74			
Dry gas base	62				64				64			
Content + temperature	E10	160	170	171	E11	193	223	226	E12	185	201	197
Temperature		151				190				169		
Content		155	163	165		197	231	232		160	176	172
Dry gas + vapor base		147	147	147		195	195	195		147	147	147
Temperature	69				76				76			
Dry gas base	66				78				67			
Content + temperature	E13	175	186	171	E14	188	185	189	E15	189	200	195
Temperature		156				158				164		
Content		158	168	156		146	145	148		160	171	165
Dry gas + vapor base		142	142	142		123	123	123		139	139	139
Temperature	76				76				75			
Dry gas base	69				60				64			

the baseline. We then held the temperature fixed to its baseline value and allowed the water vapor to vary across the intrusion, which led to an average RRTM LW computed irradiance of 142 $W m^{-2}$ (Fig. 10, green dot in subcolumn 2 for event 2), an increase of 27 $W m^{-2}$ over the baseline. With both temperature and water vapor path varying over the intrusion, the averaged RRTM LW computed irradiance was 184 $W m^{-2}$ (Fig. 10, black dot in subcolumn 2 for event 2), an increase of 69 $W m^{-2}$ over the baseline. These results are in line with the results of Persson et al. (2017) and Doyle et al. (2011), who found comparable contributions to increased surface downwelling longwave irradiance during an intrusion event as a result of increased temperature and water vapor amounts.

We performed a series of RRTM LW computations to assess the impacts of liquid and ice water during an intrusion event, separately from temperature and combined with temperature. Once again considering event 2, we first set the atmospheric pressure, temperature, and relative humidity to their baseline clear-sky values at 0600 UTC on day 78, the first 1-min interval of the intrusion event. We then allowed the liquid hydrometeors, as retrieved, to vary across event 2 while holding everything else to their baseline values. The resulting averaged RRTM LW computed surface downwelling longwave irradiance was 145 $W m^{-2}$ (Fig. 10, red dot in subcolumn 3 for event 2). The same experiment for ice hydrometeors led to a value of 140.0 $W m^{-2}$ (Fig. 10, blue dot in subcolumn 4 for event 2). Relative to the baseline value of 115 $W m^{-2}$ for dry gas plus water vapor, including liquid and ice hydrometeors led to enhancements of 30 and 25 $W m^{-2}$, respectively, which are similar to each other and to our estimate of the enhancement of 27 $W m^{-2}$ that resulted from water vapor changes at fixed temperature. Fixing atmospheric pressure and water vapor content while allowing temperature to vary with liquid and ice water led to RRTM LW computed surface downwelling longwave irradiances averaged over the period of 191 and 182 $W m^{-2}$, respectively (Fig. 10, black dots in subcolumns 3 and 4, respectively, for event 2); that is, the temperature increase during the period enhanced the computed surface downwelling longwave irradiances by 46 and 42 $W m^{-2}$ over the values obtained from the liquid- and ice-water variations at fixed temperature. The overall RRTM LW estimated enhancements in surface irradiance of 76 and 67 $W m^{-2}$ as a result of combined temperature,

TABLE 3. Time mean percentages of hydrometeor fractions (HF) and percentage increases in hydrometeor fractions (HF) and $\sigma_{SB}T^4$ for the lower, middle, and upper layers for a one-standard-deviation increase in surface downwelling longwave irradiance. The three layers are defined by the ranges in σ_P provided, where σ_P is defined as the value of the pressure at some height divided by the surface pressure. The bold numbers in parentheses are from Flournoy et al. (2016).

	Lower ($\sigma_P > 0.80$)	Middle ($0.80 \geq \sigma_P > 0.45$)	Upper ($0.45 \geq \sigma_P$)
Hydrometeor fractions (HF)			
Total	87.5% (**~75%**)	53.5% (**~30%**)	31.4% (**~30%**)
Liquid	42.4%	21.0%	3.1%
Ice	84.9%	50.5%	29.4%
Regression on HF			
Total	7.3% (**~ −5%**)	18.8% (**~8%**)	14.6% (**~12%**)
Liquid	18.8%	10.6%	1.0%
Ice	7.4%	17.7%	14.2%
Regression on $\sigma_{SB}T^4$	16.7 (**~13**) W m^{-2}	9.2 (**~8**) W m^{-2}	2.4 (**~4**) W m^{-2}

liquid-water, and ice-water changes are within the range of values reported by Persson et al. (2017). The overall results for intrusion event 2 indicate that temperature, water vapor, liquid-water, and ice-water changes produced comparable changes in the surface downwelling longwave irradiance.

Figure 10 illustrates the results of the analysis for the first six intrusion events, and Table 2 provides the same information for all 15 intrusion events. Adding water vapor to the dry gas usually more than doubled the RRTM LW computed surface downwelling longwave irradiances; these increases ranged from 58 to 117 W m^{-2} across the 15 events. Changes in water vapor, liquid water, ice water, and temperature from the dry gas and water vapor baselines for the events led to surface irradiance increases ranging from −2 to 76 W m^{-2} (Table 2, "Content + temperature" minus "Dry gas + vapor base") with the −2 W m^{-2} resulting from a small temperature drop from the beginning to end of event 11 (Table 2, E11). Overall, water vapor, liquid water, and ice water changes, together with their associated temperature changes, led to comparable changes in the surface downwelling longwave irradiance, with different quantities being dominant from one event to the next.

c. *Revisit of Flournoy et al. (2016)*

In a recent study, Flournoy et al. (2016) examined surface downwelling longwave irradiance for 17 winter seasons using ECMWF ERA-Interim reanalysis data and surface downwelling longwave irradiance measurements at Utqiaġvik, Alaska, and Ny-Ålesund, Norway. They found that surface downwelling longwave irradiance was positively correlated with middle and upper layer cloud fraction and temperature, as well as lower layer temperature. Cloud-fraction changes were not as important in the lower layer because this layer had high cloud fractions with relatively smaller fractional changes. While their use of ECMWF ERA-Interim cloud-layer output precluded them from determining which atmospheric constituents contributed most to the increased surface downwelling longwave irradiance, their results raised the possibility that elevated concentrations of ice hydrometeors in the middle to upper troposphere may be an important contributor.

As Figs. 2 and 3 illustrate, the episodic warm, moist air intrusions into the Arctic and over Utqiaġvik were deep. In addition, Fig. 4 (as well as Figs. S1 and S2 in the online supplemental material) indicates that liquid hydrometeors extended up to 5–6 km and ice hydrometeors to 8–10 km. Although the analysis period considered by Flournoy et al. (2016) differs from that considered in this study, because data from the same location (Utqiaġvik, Alaska) were used in both studies, it is worth revisiting Flournoy et al. (2016) to determine if their model-based results agree with the observations and if upper-level cloudiness contributes to the surface downwelling longwave irradiance. For this purpose, we divided each 1-min vertical profile into lower, middle, and upper segments (or layers) using σ_P coordinates (see Table 3), where σ_P is the ratio of pressure at any altitude to the surface pressure. If a 1-min segment contained a hydrometeor at any vertical location within it, we considered the layer associated with it to have a hydrometeor fraction of 1; otherwise, the hydrometeor fraction was set to 0. To calculate the daily hydrometeor fraction for each layer, we summed the 1-min hydrometeor fractions for each day and divided by 1440, the total number of 1-min hydrometeor fractions per day. We computed these daily fractions for only liquid hydrometeors, only ice hydrometeors, or both hydrometeors, which we refer to as daily liquid, ice, or total hydrometeor fractions (HF), respectively. We also averaged the temperatures within each layer over a day to create a daily averaged temperature for each layer. The liquid-dominated HSRL returns came from horizontally layered structures from which liquid precipitation was not evident. These daily liquid-water hydrometeor fractions are equivalent to daily liquid-water cloud fractions. The ice hydrometeors

TABLE 4. (column 1) The number of 1-min intervals from all 15 intrusion events with columns containing only ice, only liquid, and both liquid and ice. The average increase in surface downwelling longwave irradiances above the clear-sky baseline irradiances over all 15 intrusion events obtained by adding (column 2) the low layer of hydrometeors to the clear sky, (column 3) the low and middle layers of hydrometeors to the clear sky, and (column 4) the low, middle, and high hydrometeor layers to the clear sky.

	Samples	Baseline to low	Low to low + mid	Low + mid- to low + mid + high
Ice columns	123 521	42.17 W m^{-2}	10.66 W m^{-2}	0.51 W m^{-2}
Liquid columns	6075	57.73 W m^{-2}	0.19 W m^{-2}	0.04 W m^{-2}
Ice + liquid columns	174 909	87.64 W m^{-2}	12.65 W m^{-2}	0.22 W m^{-2}

were often extended both horizontally and vertically, and we made no attempt in this study to partition them into clouds (i.e., ice hydrometeors with little to no vertical movement) or precipitation (i.e., ice hydrometeors with significant downward motion). Also, it should be noted that Flournoy et al. (2016) did not separate cloud fraction into liquid water and ice water contributions.

We regressed daily values of $\sigma_{SB}T^4$ and hydrometeor fractions within each layer with the daily averaged surface downwelling longwave irradiance. Here, T represents the daily averaged temperature in a layer, while σ_{SB} is the Stefan-Boltzmann constant (not to be confused with the vertical pressure coordinate σ_P). The regressed values in $\sigma_{SB}T^4$ and hydrometeor fractions for the lower, middle, and upper layers are associated with a one-standard-deviation increase in surface downwelling longwave irradiance. In contrast to Flournoy et al. (2016), who regressed ERA-Interim reanalysis output with the surface downwelling longwave irradiance measurements, we used 1-min resolution hydrometeor and thermodynamic observational data collected at Utqiaġvik and averaged to daily values (Table 3). Our results for $\sigma_{SB}T^4$ exhibited similar changes from the lower to upper layers as those in Flournoy et al. (2016) but with a larger range of values: 16.7 W m^{-2} for the lower layer, 9.2 W m^{-2} for the middle layer, and 2.4 W m^{-2} for the upper layer compared to Flournoy et al.'s values of 13, 8, and 4 W m^{-2}, respectively. These findings provide observational support for the association in the ECMWF ERA-Interim output of warming in all three layers (especially for the lower two layers) during the intrusions with an increase in surface downwelling longwave irradiance.

The hydrometeor fractions averaged over the 1087-day study period in the lower, middle, and upper layers were 87.5%, 53.5%, and 31.4% as compared to the cloud fractions of 75%, 30%, and 30% in Flournoy et al. (2016). One possible explanation for these differences is the different analysis periods. Another possible explanation is the inherent difference between a spatial cloud fraction over an area, as in the reanalysis, and a temporal cloud fraction over a point, as for the observations. Also, the larger observed hydrometeor fractions compared to Flournoy et al. (2016) were likely the result of atmospheric ice hydrometeors, because the observed ice-hydrometeor fractions were nearly identical to the total hydrometeor fractions. That is, when liquid hydrometeors were present, they were nearly always in columns containing ice (Figs. 4c,d). The changes in total lower, middle, and upper layer hydrometeor fractions of 7.3%, 18.8%, and 14.6% for a one-standard-deviation increase in surface downwelling longwave irradiance were similar to those in Flournoy et al. (2016) in that the changes in the middle- and upper-layer hydrometeor fractions were much greater than that for the lower layer hydrometeors. However, an increase of 18.8% in the lower layer liquid-hydrometeor fraction rivaled the increase in ice-hydrometeor fractions in the upper two layers. This is perhaps not surprising given that, for the case study period, the lower layer liquid-hydrometeor fraction was 42.4%, with much greater values during the intrusions (Fig. 4c). The positive correlation of ice hydrometeors in the upper two layers with the surface downwelling longwave irradiance is consistent with the findings of Curry and Ebert (1992) on the importance of deep columns of atmospheric ice. The positive correlation between lower layer liquid-hydrometeor fractions and surface downwelling longwave irradiance is perhaps better known and was pointed out by both Curry and Ebert (1992) and Shupe and Intrieri (2004).

The positive correlations between $\sigma_{SB}T^4$ in all layers and surface downwelling longwave irradiance are consistent with earlier results presented in section 3b, demonstrating that increased temperatures throughout the atmospheric column during intrusion events may lead to enhancements in the surface downwelling longwave irradiance. One question that arises in this regard is the source of the increased surface downwelling longwave irradiance: is it coming exclusively from the lower layer, or do the middle and upper layers contribute as well?

To answer this question, we ran RRTM LW on every 1-min vertical profile composing the 15 intrusion events with hydrometeors present only in the lower layer, only in the lower and middle layers, and in all three layers. We further refined the results by separating each group into ice only vertical profiles, liquid only vertical profiles, and mixed (liquid and ice) vertical profiles. We then computed the average over all 15 intrusion events. The results are presented in Table 4.

As Table 4 (column 1) illustrates, the intrusion events were dominated by mixed phase and pure ice profiles, with few pure liquid profiles. The baseline irradiances were the RRTM LW computed clear-sky irradiances at the first time of each intrusion event, just as for the results in Table 2 ("Vap" columns and "Dry gas + vapor base" rows). Adding ice, liquid, and ice plus liquid (mixed) hydrometeors in the lower layer to the RRTM LW computations increased the surface downwelling longwave irradiances by 42.17, 57.73, and 87.64 $W m^{-2}$, respectively, over their baseline values, attesting to the importance of hydrometeors when they occurred. Adding the middle layer of hydrometeors to the lower layer increased the surface irradiance by an additional 10.66 $W m^{-2}$ (20.2% of the total) and 12.65 $W m^{-2}$ (12.6% of the total) for the ice and mixed profiles, but only 0.19 $W m^{-2}$ for the liquid profiles. The impact of the upper layer was small in all cases. These results indicate that the presence of ice in the middle layer was a causative agent of the increase in surface downwelling longwave irradiance, whereas ice in the upper layer was not. Therefore, the increases in surface downwelling longwave irradiance are primarily from the bottom two layers.

In summary, the intrusion events were associated with columns of elevated temperature, water vapor content, liquid water, and ice water. The temperature regressions of Flournoy et al. (2016), based on ECMWF ERA-Interim reanalysis output, are consistent with the observed elevated temperatures present in all layers during the intrusions. The deep columns of ice in the observations were accompanied by increases in temperature, moisture, and water contents throughout the column. The surface downwelling longwave irradiance was sensitive to their changes in the lower and middle layers, but not the upper layer. These results imply that even though a large amount of upper layer ice accompanies the events, consistent with the strong correlations between upper layer cloud fraction and surface irradiance found by Flournoy et al. (2016), these ice hydrometeors have little influence on surface irradiance during the events.

4. Discussion and conclusions

In this study, results from radiative transfer calculations are presented in an attempt to investigate the effects of temperature, water vapor, liquid water, and ice water on surface downwelling longwave irradiance at the DOE ARM User Facility in Utqiaġvik, Alaska, for the months of November through April for the six winter seasons from 2013/14 through 2018/19. The analysis revealed that during the study period water vapor was, on average, the most important contributor to the surface irradiance amongst all constituents. During the individual intrusion events, however, individual contributions from temperature, water vapor, liquid water, and ice water were comparable to each other. This was the result of increases in column water vapor and temperature during the intrusion events accompanied by more intermittent liquid, ice, and mixed phase hydrometeors. The RRTM LW computations, with the observed temperature and all three phases of water as input, yielded surface downwelling longwave irradiance values that matched with observed irradiances within an accuracy of −0.8%. Repeating the RRTM LW computations with the observed liquid and ice water artificially removed demonstrated that temperature and water vapor alone accounted for 83.2% of the total surface irradiance on average during the 1087-day period. Including either liquid water or ice water brought the calculated surface irradiance values to within about 11–17 $W m^{-2}$, or ~92%–95%, of the observed value on average. That is, the addition of either liquid water or ice water to the water vapor was sufficient to explain 92%–95% of the observed surface irradiance, indicating that both liquid water and ice water are needed to account for the remaining 5%–8%. RRTM LW computations performed without inclusion of water vapor produced only 74.1% of the observed surface irradiance on average. At least for this particular case study period, combined liquid- and ice-water amounts were insufficient to make up for water vapor optical depths outside of the 8–12-μm region of the spectrum when water vapor was removed. Our findings are in line with earlier studies by Curry et al. (1995), Doyle et al. (2011), and Town et al. (2005) on how increasing water vapor and temperature significantly enhance the surface downwelling longwave irradiance in polar regions. In contrast to these previous studies, we were also able to quantify the importance to the surface downwelling longwave irradiance of the water vapor relative to the liquid and ice water, and their vertical layering, by taking advantage of the availability of more complete datasets at the DOE ARM User Facility.

There are numerous possible sources of error in the RRTM LW computations that we performed. We neglected scattering in the RRTM LW computations, incurring an expected underestimate of about 1 $W m^{-2}$ in the surface downwelling longwave irradiance based on existing literature. Interpolating temperatures to 1-min sampling from 6-hourly soundings comes with error, and we did not attempt to quantify the consequences of this error. We did find evidence for a slow, small-magnitude drift in the microwave radiometer retrieved water vapor path that led to a small low bias in the RRTM LW surface downwelling longwave irradiance computations by the end of the 6-yr period. We did not attempt to incorporate aerosols into the RRTM LW computations, and retrieving liquid-water content

profiles remains problematic, making assumptions about them necessary; in our study, we assumed adiabatic liquid water contents. Finally, our treatment of ice particles as spheres in both the ice-particle retrievals and the RRTM LW computations introduced numerous sources of uncertainty as well. Yet, the resulting RRTM LW surface downwelling longwave irradiances had a low bias of $-1.7\,\mathrm{W\,m^{-2}}$ and a root-mean-square difference of $5.83\,\mathrm{W\,m^{-2}}$ relative to the observations, both of which are small compared to differences obtained by neglecting an atmospheric constituent in the RRTM LW computations. We infer from these results that the HSRL-measured optical depths in the presence of hydrometeors placed a strong constraint on the RRTM LW computations of surface downwelling longwave irradiance. Several design features of the HSRL, including its narrow field-of-view of 45 μrad, which suppresses multiple scattering effects, make it a valuable asset in hydrometeor-retrieval research (Eloranta 2005, 2016).

The DOE ARM User Facility observations also revealed that water vapor fluctuations occurred over 1- to 2-week time periods, whereas the ice-water fluctuations were dominated by higher frequencies, typically over a few days. Liquid water was also intermittent, and typically occurred within ice-water-containing columns. This result raises the possibility that the water vapor fluctuations were driven by slowly evolving planetary-scale waves, while the liquid and ice water variability arose from shorter time scale processes such as synoptic- or mesoscale features that were embedded in the planetary-scale waves. This possibility is, in fact, consistent with previous findings that planetary-scale wave activity is often followed by Arctic warming (Yoo et al. 2012; Liu and Barnes 2015; Baggett et al. 2016; Goss et al. 2016) while shorter length scale waves are much less effective at warming the Arctic (Baggett and Lee 2015, 2017). This interpretation is also consistent with the moisture-flux convergence shown in Newman et al. (2012); over much of Alaska during the cold season, moisture-flux convergence by low-frequency (planetary scale) waves is greater than that from synoptic-scale eddies. The consistency of these findings indicates that additional attention needs to be given to planetary-scale wave dynamics and the waves' impact on the Arctic system via water vapor, temperature, and hydrometeor changes and their feedbacks.

Acknowledgments. E. Clothiaux's contribution to this research was funded by subcontract 300324 of The Pennsylvania State University with the Brookhaven National Laboratory in support of the ARM-ASR Radar Science Group. The contribution to this research by Sukyoung Lee and Steven Feldstein was funded by National Science Foundation Grant OPP-1723832. Data were obtained from the Atmospheric Radiation Measurement (ARM) User Facility, a U.S. Department of Energy (DOE) Office of Science user facility managed by the Office of Biological and Environmental Research. The five anonymous reviewers of the paper provided detailed, thorough comments and suggestions that enriched substantially the content of the paper. The editor, Xianglei Huang, was gracious in allowing the time necessary to deal meaningfully with all of the reviewer comments.

REFERENCES

Andreas, A., M. Dooraghi, A. Habte, M. Kutchenreiter, I. Reda, and M. Sengupta, 2018: Solar Infrared Radiation Station (SIRS), Sky Radiation (SKYRAD), Ground Radiation (GNDRAD), and Broadband Radiometer Station (BRS) Instrument Handbook. Office of Science, U.S. Department of Energy Tech. Rep. DOE/SC-ARM-TR-025, 58 pp., https://www.arm.gov/publications/tech_reports/handbooks/sirs_handbook.pdf.

Baggett, C., and S. Lee, 2015: Arctic warming induced by tropically forced tapping of available potential energy and the role of the planetary-scale waves. *J. Atmos. Sci.*, **72**, 1562–1568, https://doi:10.1175/JAS-D-14-0334.1.

——, and ——, 2017: An identification of the mechanisms that lead to Arctic warming during planetary-scale and synoptic-scale wave life cycles. *J. Atmos. Sci.*, **74**, 1859–1877, https://doi:10.1175/JAS-D-16-0156.1.

——, ——, and S. B. Feldstein, 2016: An investigation of the presence of atmospheric rivers over the North Pacific during planetary-scale wave life cycles and their role in Arctic warming. *J. Atmos. Sci.*, **73**, 4329–4347, https://doi.org/10.1175/JAS-D-16-0033.1.

Curry, J. A., and E. E. Ebert, 1992: Annual cycle of radiation fluxes over the Arctic Ocean: Sensitivity to cloud optical properties. *J. Climate*, **5**, 1267–1280, https://doi.org/10.1175/1520-0442(1992)005<1267:ACORFO>2.0.CO;2.

——, J. L. Schramm, M. C. Serreze, and E. E. Ebert, 1995: Water vapor feedback over the Arctic Ocean. *J. Geophys. Res.*, **100**, 14 223–14 229, https://doi.org/10.1029/95JD00824.

Dong, X., B. Xi, K. Crosby, C. N. Long, R. S. Stone, and M. D. Shupe, 2010: A 10 year climatology of Arctic cloud fraction and radiative forcing at Barrow, Alaska. *J. Geophys. Res.*, **115**, D17212, https://doi.org/10.1029/2009JD013489.

Donovan, D. P., and A. C. A. P. van Lammeren, 2001: Cloud effective particle size and water content profile retrievals using combined lidar and radar observations: 1. Theory and examples. *J. Geophys. Res.*, **106**, 27 425–27 448, https://doi.org/10.1029/2001JD900243.

Doyle, J. G., G. Lesins, C. P. Thackray, C. Perro, G. J. Nott, T. J. Duck, R. Damoah, and J. R. Drummond, 2011: Water vapor intrusions into the High Arctic during winter. *Geophys. Res. Lett.*, **38**, L12806, https://doi.org/10.1029/2011GL047493.

Eloranta, E. W., 2005: High spectral resolution lidar. *Lidar: Range-Resolved Optical Remote Sensing of the Atmosphere*, C. Weitkamp, Ed., Springler-Verlag, 456 pp.

——, 2016: Drizzle measurements using high spectral resolution lidar and radar data. *EPJ Web Conf.*, **119**, 21003, https://doi.org/10.1051/EPJCONF/201611921003.

Flournoy, M. D., S. B. Feldstein, S. Lee, and E. E. Clothiaux, 2016: Exploring the tropically excited Arctic warming mechanism with station data: Links between tropical convection and

Arctic downward infrared radiation. *J. Atmos. Sci.*, **73**, 1143–1158, https://doi.org/10.1175/JAS-D-14-0271.1.

Goldsmith, J., 2016: High spectral resolution lidar instrument handbook. Office of Science, U.S. Department of Energy Tech. Rep. DOE/SC-ARM/TR-157, 17 pp., https://www.arm.gov/publications/tech_reports/handbooks/hsrl_handbook.pdf.

Gong, T., S. Feldstein, and S. Lee, 2017: The role of downward infrared radiation in the recent Arctic winter warming trend. *J. Climate*, **30**, 4937–4949, https://doi.org/10.1175/JCLI-D-16-0180.1.

Goss, M., S. B. Feldstein, and S. Lee, 2016: Stationary wave interference and its relation to tropical convection and Arctic warming. *J Climate*, **29**, 1369–1389, https://doi:10.1175/JCLI-D-15-0267.1.

Graversen, R. G., and M. Burtu, 2016: Arctic amplification enhanced by latent energy transport of atmospheric planetary waves. *Quart. J. Roy. Meteor. Soc.*, **142**, 2046–2054, https://doi.org/10.1002/qj.2802.

Gröbner, J., I. Reda, S. Wacker, S. Nyekl, K. Behrens, and J. Gorman, 2014: A new absolute reference for atmospheric longwave irradiance measurements with traceability to SI units. *J. Geophys. Res. Atmos.*, **119**, 7083–7090, https://doi.org/10.1002/2014JD021630.

Hu, Y. X., and K. Stamnes, 1993: An accurate parameterization of the radiative properties of water clouds suitable for use in climate models. *J. Climate*, **6**, 728–742, https://doi.org/10.1175/1520-0442(1993)006<0728:AAPOTR>2.0.CO;2.

Iacono, M. J., E. J. Mlawer, S. A. Clough, and J.-J. Morcrette, 2000: Impact of an improved longwave radiation model, RRTM, on the energy budget and thermodynamic properties of the NCAR community climate model, CCM3. *J. Geophys. Res.*, **105**, 14 873–14 890, https://doi.org/10.1029/2000JD900091.

Key, J. R., 2002: Streamer Version 3.0 User's Guide. Cooperative Institute for Meteorological Satellite Studies, University of Wisconsin, 70 pp., https://stratus.ssec.wisc.edu/streamer/userman.pdf.

Kuo, C.-P., P. Yang, X. Huang, D. Feldman, M. Flanner, C. Kuo, and E. J. Mlawer, 2017: Impact of multiple scattering on longwave radiative transfer involving clouds. *J. Adv. Model. Earth Syst.*, **9**, 3082–3098, https://doi.org/10.1002/2017MS001117.

Lamer, K., A. M. Fridlind, A. S. Ackerman, P. Kollias, E. E. Clothiaux, and M. Kelley, 2018: $(GO)^2$-SIM: A GCM-oriented ground-observation forward-simulator framework for objective evaluation of cloud and precipitation phase. *Geosci. Model Dev.*, **11**, 4195–4214, https://doi.org/10.5194/gmd-11-4195-2018.

Lee, S., T. Gong, N. Johnson, S. B. Feldstein, and D. Pollard, 2011: On the possible link between tropical convection and the Northern Hemisphere Arctic surface air temperature change between 1958 and 2001. *J. Climate*, **24**, 4350–4367, https://doi.org/10.1175/2011JCLI4003.1.

——, ——, S. B. Feldstein, J. A. Screen, and I. Simmonds, 2017: Revisiting the cause of the 1989–2009 Arctic surface warming using the surface energy budget: Downward infrared radiation dominates the surface fluxes. *Geophys. Res. Lett.*, **44**, 10 654–10 661, https://doi.org/10.1002/2017GL075375.

Liu, C., and E. A. Barnes, 2015: Extreme moisture transport into the Arctic linked to Rossby wave breaking. *J. Geophys. Res. Atmos.*, **120**, 3774–3788, https://doi.org/10.1002/2014JD022796.

Mlawer, E. J., S. J. Taubman, P. D. Brown, M. J. Iacono, and S. A. Clough, 1997: Radiative transfer for inhomogeneous atmospheres: RRTM, a validated correlated-*k* model for the longwave. *J. Geophys. Res.*, **102**, 16 663–16 682, https://doi.org/10.1029/97JD00237.

Newman, M., G. N. Kiladis, K. M. Weickmann, F. M. Ralph, and P. D. Sardeshmukh, 2012: Relative contributions of synoptic and low-frequency eddies to time-mean atmospheric moisture transport, including the role of atmospheric rivers. *J. Climate*, **25**, 7341–7361, https://doi.org/10.1175/JCLI-D-11-00665.1.

Park, H.-S., S. Lee, S.-W. Son, S. B. Feldstein, and Y. Kosaka, 2015: The impact of poleward moisture and sensible heat flux on Arctic winter sea ice variability. *J. Climate*, **28**, 5030–5040, https://doi.org/10.1175/JCLI-D-15-0074.1.

Persson, P. O. G., M. D. Shupe, D. Perovich, and A. Solomon, 2017: Linking atmospheric synoptic transport, cloud phase, surface energy fluxes, and sea-ice growth: Observations of midwinter SHEBA conditions. *Climate Dyn.*, **49**, 1341–1364, https://doi.org/10.1007/s00382-016-3383-1.

Petty, G. W., and W. Huang, 2011: The modified gamma size distribution applied to inhomogeneous and nonspherical particles: Key relationships and conversions. *J. Atmos. Sci.*, **68**, 1460–1473, https://doi.org/10.1175/2011JAS3645.1.

Reda, R., J. Zeng, J. Scheuch, L. Hanssen, B. Wilthan, D. Myers, and T. Stoffel, 2012: An absolute cavity pyrgeometer to measure the absolute outdoor longwave irradiance with traceability to international system of units, SI. *J. Atmos. Sol.-Terr. Phys.*, **77**, 132–143, https://doi.org/10.1016/j.jastp.2011.12.011.

Shupe, M. D., 2007: A ground-based multisensor cloud phase classifier. *Geophys. Res. Lett.*, **34**, L22809, https://doi.org/10.1029/2007GL031008.

——, and J. M. Intrieri, 2004: Cloud radiative forcing of the Arctic surface: The influence of cloud properties, surface albedo, and solar zenith angle. *J. Climate*, **17**, 616–628, https://doi.org/10.1175/1520-0442(2004)017<0616:CRFOTA>2.0.CO;2.

——, D. D. Turner, A. Zwink, M. M. Thieman, E. J. Mlawer, and T. Shippert, 2015: Deriving Arctic cloud microphysics at Barrow, Alaska: Algorithms, results, and radiative closure. *J. Appl. Meteor. Climatol.*, **54**, 1675–1689, https://doi.org/10.1175/JAMC-D-15-0054.1.

Silber, I., J. Verlinde, E. W. Eloranta, C. J. Flynn, and D. M. Flynn, 2018: Polar liquid cloud base detection algorithms for high spectral resolution or micropulse lidar data. *J. Geophys. Res. Atmos.*, **123**, 4310–4322, https://doi.org/10.1029/2017JD027840.

Skific, N., and J. A. Francis, 2013: Drivers of projected change in Arctic moist static energy transport. *J. Geophys. Res. Atmos.*, **118**, 2748–2761, https://doi.org/10.1002/JGRD.50292.

Smith, W. L., X. L. Ma, S. A. Ackerman, H. E. Revercomb, and R. O. Knuteson, 1993: Remote sensing cloud properties from high spectral resolution infrared observations. *J. Atmos. Sci.*, **50**, 1708–1720, https://doi.org/10.1175/1520-0469(1993)050<1708:RSCPFH>2.0.CO;2.

Stephens, G. L., 1978: Radiation profiles in extended water clouds. I: Theory. *J. Atmos. Sci.*, **35**, 2111–2122, https://doi.org/10.1175/1520-0469(1978)035<2111:RPIEWC>2.0.CO;2.

Tang, G., P. Yang, G. W. Kattawar, X. Huang, E. J. Mlawer, B. A. Baum, and M. D. King, 2018: Improvement of the simulation of cloud longwave scattering in broadband radiative transfer models. *J. Atmos. Sci.*, **75**, 2217–2233, https://doi.org/10.1175/JAS-D-18-0014.1.

Town, M. S., V. P. Walden, and S. G. Warren, 2005: Spectral and broadband longwave downwelling radiative fluxes, cloud radiative forcing, and fractional cloud cover over the South Pole. *J. Climate*, **18**, 4235–4252, https://doi.org/10.1175/JCLI3525.1.

Troyan, D., 2012: Merged sounding value-added product. Office of Science, U.S. Department of Energy Tech. Rep. DOE/SC-ARM/TR-087, 19 pp., https://www.arm.gov/publications/tech_reports/doe-sc-arm-tr-087.pdf.

Turner, D. D., B. M. Lesht, S. A. Clough, J. C. Liljegren, H. E. Revercomb, and D. C. Tobin, 2003: Dry bias and variability in

Vaisala RS80-H radiosondes: The ARM experience. *J. Atmos. Oceanic Technol.*, **20**, 117–132, https://doi.org/10.1175/1520-0426(2003)020<0117:DBAVIV>2.0.CO;2.

——, and Coauthors, 2007a: Thin liquid water clouds: Their importance and our challenge. *Bull. Amer. Meteor. Soc.*, **88**, 177–190, https://doi.org/10.1175/BAMS-88-2-177.

——, S. A. Clough, J. C. Liljegren, E. E. Clothiaux, K. E. Cady-Pereira, and K. L. Gaustad, 2007b: Retrieving liquid water path and precipitable water vapor from the Atmospheric Radiation Measurement (ARM) microwave radiometers. *IEEE Trans. Geosci. Remote Sens.*, **45**, 3680–3690, https://doi.org/10.1109/TGRS.2007.903703.

Wang, Z., and K. Sassen, 2001: Cloud type and macrophysical property retrieval using multiple remote sensors. *J. Appl. Meteor.*, **40**, 1665–1682, https://doi.org/10.1175/1520-0450(2001)040<1665:CTAMPR>2.0.CO;2.

Widener, K., N. Bharadwaj, and K. Johnson, 2012: Ka-Band ARM Zenith Radar (KAZR). Office of Science, U.S. Department of Energy Tech. Rep. DOE/SC-ARM/TR-106, 25 pp., https://www.arm.gov/publications/tech_reports/handbooks/kazr_handbook.pdf.

Woods, C., and R. Caballero, 2016: The role of moist intrusions in winter Arctic warming and sea ice decline. *J. Climate*, **29**, 4473–4485, https://doi.org/10.1175/JCLI-D-15-0773.1.

——, ——, and G. Svensson, 2013: Large-scale circulation associated with moisture intrusions into the Arctic during winter. *Geophys. Res. Lett.*, **40**, 4717–4721, https://doi.org/10.1002/grl.50912.

Yoo, C., S. Lee, and S. B. Feldstein, 2012: Mechanisms of Artic surface air temperature change in response to the Madden–Julian oscillation. *J. Climate*, **25**, 5777–5790, https://doi.org/10.1175/JCLI-D-11-00566.1.